Heliyon 10 (2024) e31109

Contents lists available at ScienceDirect

Heliyon

journal homepage: www.cell.com/heliyon

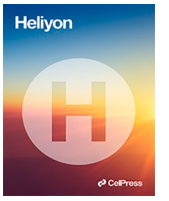

Research article

Synergistic effect of ZnO/Ag_2O@g-C_3N_4 based nanocomposites embedded in carrageenan matrix for dye degradation in water

Feziwe B. Mamba [a,b,c], Bhekani S. Mbuli [a,b,c], James Ramontja [a,b,c,*]

[a] Department of Chemical Sciences, Faculty of Science, University of Johannesburg, P.O. Box 17011, Doornfontein, Johannesburg, 2028, South Africa
[b] DSI/Mintek Nanotechnology Innovation Centre, University of Johannesburg, Doornfontein, 2028, South Africa
[c] Centre for Nanomaterials Science Research, University of Johannesburg, Doornfontein, 2028, South Africa

ARTICLE INFO

Keywords:
Graphitic carbon nitride
Carrageenan
Nanocomposite
Nanomaterial
Visible light
Photocatalysis

ABSTRACT

This research achieved success by synthesizing innovative nanocomposite composed of zinc oxide (ZnO), graphitic carbon nitride (g-C_3N_4) and silver oxide (Ag_2O) nanomaterials incorporated into a carrageenan matrix, thus creating an environmentally friendly and stable support structure. The synthesis process involved hydrothermal and chemical precipitation methods to create photocatalytic g-C_3N_4, ZnO, and Ag_2O nanocomposites. The success is evident through the characterization results, which unveiled distinctive peaks corresponding to Zn–O (590-404 cm^{-1}) and Ag–O (2072 cm^{-1}) stretching in the Fourier transform infrared (FTIR) and X-ray diffraction (XRD) analyses, conclusively confirming the successful synthesis of g-C_3N_4, ZnO, Ag_2O, and their respective nanocomposites. Further validation through a scanning electron microscope coupled with an energy dispersive spectrometer (SEM-EDX) and elemental mapping affirmed the presence of Zn, O, Ag, C, and N. Additionally, transmission electron microscope (TEM) imaging unveiled the nanosheet morphology of g-C_3N_4, the nanorod structure of ZnO, and the spherical form of Ag_2O nanomaterials. ZnO and Ag_2O nanomaterials demonstrated a consistent 10–20 nm size range. To underscore their ability to harness visible light, the nanomaterials were excited at 380 nm, emitting visible light emission within the 400–450 nm range. The synthesized nanocomposites showcased outstanding adsorption and photocatalytic properties, achieving efficiency ranging from 80 % to 98 %, attributed to the synergistic interactions between the various components. These findings culminate in a confirmation of the research's success, validating the exceptional potential of these nanocomposites for various applications.

1. Introduction

The textile industry produces a significant amount of wastewater contaminated with dyes. These dyes can affect the water's light penetration, colour, odour, and pH. The chemicals in textile wastewater have been linked to various health challenges, including allergies, dermatitis, cancer, and genetic mutations. Unfortunately, most dyes are difficult to break down. Thus, they remain in the environment for long [1–6]. The major challenges associated with dye degradation are the persistence of dyes in wastewater, their potential environmental and health hazards, and the limited efficiency of conventional treatment methods. Traditional methods of dye

* Corresponding author. Department of Chemical Sciences, Faculty of Science, University of Johannesburg, P.O. Box 17011, Doornfontein, Johannesburg, 2028, South Africa.
E-mail address: jamesr@uj.ac.za (J. Ramontja).

https://doi.org/10.1016/j.heliyon.2024.e31109
Received 25 January 2024; Received in revised form 2 May 2024; Accepted 9 May 2024
Available online 10 May 2024

degradation, such as biological treatment or chemical oxidation, often suffer from limitations such as slow degradation rates, incomplete removal of dyes, and the generation of harmful by-products. There is a growing need for advanced nanomaterials that can efficiently degrade a wide range of dye pollutants with improved performance and environmental sustainability. Introducing nanocomposites in dye degradation processes offers several advantages, including increased surface area, enhanced catalytic activity, and the ability to target specific dye molecules. However, challenges remain in optimizing the design and synthesis of these nanocomposites for maximum efficiency and stability [1,7–9].

Conventional water treatment technologies, including coagulation, flocculation [10–15], electrochemical treatment, adsorption, and precipitation, also present challenges such as secondary pollution like formed flocs and settled particles. The disposal of formed sludge can be expensive and less effective for highly dye-concentrated effluent [1,6,10,16]. Photocatalytic degradation presents an innovative and effective approach for water contaminant removal, operating without chemicals or gases to minimize the risk of secondary pollution. Moreover, the oxidation capacity of the photocatalytic process is robust enough to break down persistent pollutants into more basic components [17,18].

Despite the excellent treatment performance in ultraviolet (UV) photocatalysis due to its stronger intensity than solar/visible light, the large band gap of materials (between 3 eV and 5 eV) necessitates UV irradiation for successful electron excitation. However, solar/visible light photocatalysis is preferred economically and recognized as an environmentally friendly technology for pollutant removal. UV light can cause harmful effects on living organisms, including skin damage and potential DNA damage [19]. First-generation photocatalysts contain one conduction band (CB) and one valence band (VB), which is a disadvantage because it limits the range of electronic transitions and energy levels available for certain processes. Electrons are more likely to fall back into the VB without producing reactive oxygen species because multiple energy bands are missing. This can restrict the material's ability to participate in electronic interactions or reactions efficiently [17].

Photocatalysts can be modified to reduce their broadband gaps. This can be accomplished through metal and non-metal doping or coupled with carbon-based substances such as graphene carbon nanotubes and graphitic carbon nitride (g-C_3N_4) [18]. The coupling with g-C_3N_4 allows the materials to harness a broader range of the solar spectrum and utilize light energy more efficiently. A significant level of light absorption across a broad spectrum of wavelengths is also present in carbon compounds [20–22]. However, due to a lack of a high functional recombination rate, pristine g-C_3N_4 limits the high photocatalytic ability and reusability performance [10,23]. To this end, researchers have utilized different techniques, such as modification or doping, to improve the performance and tailor the properties of g-C_3N_4 [10,24].

g-C_3N_4 can be doped with metal oxides (silver (Ag), titanium dioxide (TiO_2), ZnO, Ag_2O) to enhance its photocatalytic activity and expand its applications in environmental remediation and energy conversion processes. Nanocomposites such as g-C_3N_4/Ag/TiO_2, g-C_3N_4/rGO/TiO_2, g-C_3N_4/Ag_2O/Fe_3O_4, g-C_3N_4/Co_3O_4/Ag_2O, and g-C_3N_4/C-doped with ZnO, g-C_3N_4/ZnO are reported in the literature [10,25]. ZnO has been used since it is non-toxic, effective at charge recombination, and highly photosensitive [10,26]. However, ZnO's wide band gap (3.3 eV) results in a low light utilization rate [16,26]. A higher photoluminescence (PL) intensity of ZnO indicates higher recombination and lower light energy utilization. The low separation efficiency of electron and hole pairs under visible light irradiation makes achieving an acceptable photocatalytic effect difficult, necessitating the preparation of nanocomposites [16,26].

Zhong et al. [25] demonstrated a g-C_3N_4/ZnO photocatalysis to eradicate methylene blue (MB), Rhodamine B (RhB), Cr (VI) and eosin, and achieving a photocatalytic rate of 98 % for MB. The excellent performance of the g-C_3N_4/ZnO photocatalyst was attributed to the capacity of the g-C_3N_4 to broaden the spectral range of the single ZnO absorption—also, the ability to increase the specific surface area of the nanocomposites of interest. As a result, the photocatalytic reaction region and the surface-active sites were enlarged. Furthermore, in the presence of simulated visible light, photogenerated electrons on the g-C_3N_4 conduction band migrate to the ZnO conduction band because it is lower than that of ZnO. Consequently, these phenomena prolong the electron carrier lifetime and prevent fast electron-hole recombination [25]. Balu et al. [27] focused on the use of α-Fe_2O_3 onto g-C_3N_4/ZnO, which resulted in increased visible light absorption, thus, higher efficiency in e^-/h^+ separation and better electron transfer ability. This led to improved degradation rates of tartrazine dye under visible light illumination [27].

Another photocatalyst that has been explored is Ag_2O. The use of Ag_2O is restricted by its photosensitivity and rapid recombination of photoinduced electron-hole pairs. However, Ag_2O nanomaterials are effective photocatalysts when incorporated into other nanomaterials due to their low band gap (1.3 eV) and high compatibility as a p-type semiconductor [10,16,28]. For example, Chen et al. [29] reported an enhanced photodegradation of charged pollutants under visible light in the presence of Ag_2O/g-C_3N_4 obtaining above 80 % photocatalytic activity against positively charged MB and negatively charged methyl orange dyes when exposed to visible light, but not for uncharged RhB dye [29]. Also, Kulal and Kodialbail [30] reported the incorporation of Ag_2O into AgO–TiO_2. The Ag_2O/AgO–TiO_2 nanocomposites effectively degraded Reactive Blue 220 (96 % of 100 ppm in 90 min) and 63 % degradation of methyl orange in 300 min. Additionally, Rong et al. [31] improved on this by incorporating Ag_2O into g-C_3N_4/ZnO, preparing g-C_3N_4/ZnO–Ag_2O nanocomposite, thereby resulting in a ciprofloxacin degradation rate of 97.4 % as opposed to 69.4 % when utilizing only the ZnO–Ag_2O nanocomposite [31].

In this research, the incorporation of g-C_3N_4, ZnO and Ag_2O nanomaterials, individually and in combination with the carrageenan (Carr) matrix, was designed to harness their unique attributes and synergistic effects [32,33]. Several well-justified reasons drove this approach. Firstly, g-C_3N_4 is known for its exceptional visible light absorption and photocatalytic capabilities, which are crucial for initiating chemical reactions under mild conditions, thus avoiding the need for strong reagents and high-energy UV light [34]. ZnO and Ag_2O offer high surface areas and adsorption capacities, making them effective in capturing and retaining pollutants. Incorporating these nanomaterials into the carrageenan matrix capitalizes on carrageenan's benefits, including improved stability, easier handling in water treatment, biocompatibility, structural reinforcement, and antimicrobial activity, ensuring sustainable and safe nanocomposite materials [32,33].

The synergistic effect of combining these nanomaterials within the carrageenan matrix was a key hypothesis in this research. The objective was to design nanocomposites with the dual capability of proficiently adsorbing pollutants through the substantial surface area afforded by g-C_3N_4, ZnO and Ag_2O while also demonstrating an ability for their effective degradation under visible light exposure. This combination is particularly promising for addressing water pollution concerns as it offers a multifaceted approach to water purification, allowing for both adsorption and photocatalytic degradation of contaminants.

For this study, it was envisaged that the ZnO, Ag_2O and g-C_3N_4 nanomaterials could be utilized for the removal of dyes from water to address the challenges associated with the degradation of dyes by developing novel GZA_Carr (g-C_3N_4/ZnO/Ag_2O@carrageen) nanocomposites. This is because the GZA_Carr was envisaged to possess tailored properties such as increased hydrophilicity and high surface area. Furthermore, the introduction of pendant functional groups such as sulfates was expected to increase the electron pool of the nanocomposites for enhanced dye degradation. Individually, the g-C_3N_4, ZnO and Ag_2O nanomaterials coupled with the carrageenan hydrogel are expected to be good adsorbents and/or photocatalysts. That is why when these materials were to be combined with the g-C_3N_4 nanosheets, the expectation was that they would create a synergistic effect, thereby enhancing the photocatalytic activity of the nanocomposite. This synergistic effect was anticipated to substantively increase the efficiency of dye degradation under visible light irradiation.

Furthermore, one of the limitations of traditional semiconductor photocatalysts such as ZnO is their limited response to visible light irradiation during photocatalysis. However, to supplement this limitation, the g-C_3N_4 has a suitable bandgap that allows the nanosheets to absorb visible light effectively during photocatalysis. Therefore, incorporating the ZnO and Ag_2O nanoparticles into g-C_3N_4, the resulting nanocomposites were expected to exhibit improved visible light responsiveness, thereby enabling them to degrade dyes under sunlight or visible light sources efficiently. The resultant nanocomposites cannot only be separated easily from the treated water but also recycled multiple times without significant loss of photocatalytic activity. This can then reduce the operational costs of their entire treatment system and eliminate potentially negative environmental impacts.

Above all, ZnO, Ag_2O, and g-C_3N_4 nanomaterials are known to be non-toxic, making the nanocomposites environmentally friendly compared to some alternative photocatalysts. Additionally, the incorporation of the carrageenan hydrogel was anticipated to enhance the biocompatibility of the materials to biopolymers and increase their surface area. As such, this was crucial for their water treatment applications to avoid leaching and secondary pollution and increase their compatibility with biopolymers for possible applications in water treatment. Consequently, the ZnO–Ag_2O@g-C_3N_4 nanocomposites within the carrageenan hydrogel offered a promising solution for dye removal in water treatment due to their enhanced photocatalytic activity, visible light responsiveness, high surface area, recyclability, selective adsorption capability, and environmental friendliness.

2. Experimental

2.1. Chemicals and materials

Melamine ($C_3H_6N_6$, reagent grade, ≥99.0 %), sodium hydroxide pellets (NaOH, reagent grade, ≥98.0 %, anhydrous), hydrochloric acid (HCl, analytical grade, 32 %), ethanol (C_2H_6O, analytical grade, ≥96.0 %) silver nitrate ($AgNO_3$, reagent grade, ≥99.0 %), zinc chloride ($ZnCl_2$, reagent grade, ≥98.0 %), zinc acetate dihydrate, ($Zn(CH_3COO)_2{\cdot}2H_2O$, reagent grade, ≥98.0 %), κ-carrageenan of food grade were purchased from Sigma Aldrich, South Africa and were used as received.

2.2. Synthesis of nanomaterials

2.2.1. Thermal polymerization of graphitic carbon nitride (g-C_3N_4)

g-C_3N_4 nanosheets were prepared based on a procedure described by Yuan et al., Zhang et al. and Yang et al. [35–37]. Melamine (10.00 g) was heated in a crucible at a 10 °C/min rate in a muffle furnace at 500 °C for 4 h. The resultant yellow product, bulk g-C_3N_4, was then allowed to cool to room temperature before being ground into a fine powder. To prepare nanosheets, the bulk of g-C_3N_4 was exfoliated using deionized water. This was accomplished by dispersing the bulk g-C_3N_4 in deionized water (5 mg/mL) and sonicating at room temperature to produce the nanosheets, as adapted from Yang et al. [37] and Zhang et al. [36]. The bulk g-C_3N_4 absorbed deionized water expanded, and the swollen g-C_3N_4 was then exfoliated into nanosheets during sonication. To extract the g-C_3N_4 nanosheet product, the suspension was centrifuged at 6000 rpm to settle and separate from the water solvent. The g-C_3N_4 nanosheet product was subsequently dried overnight at 70 °C and then ready for characterization and to form nanocomposites.

2.2.2. Synthesis of zinc oxide (ZnO) nanomaterials

The wet chemical method was used to synthesize the ZnO nanomaterials. This reaction involved dissolving $ZnCl_2$ (5.00 g) distilled water (50 mL). To completely dissolve the $ZnCl_2$, 3 drops of HCl (32 %) were added to the $ZnCl_2$ solution and heated to 80 °C while stirring. After that, 1.00 mol/L NaOH (40 mL) was gradually added to the solution while it was constantly stirred to produce a white precipitate of zinc hydroxide ($Zn(OH)_2$). The white mixture was then stirred for 2 h to ensure complete $Zn(OH)_2$ precipitation and kept at a pH range of 9–11 to avoid agglomeration. The white precipitate was centrifuged and washed with distilled water several times to dissolve NaCl and remove impurities. The white $Zn(OH)_2$ nanomaterials were oven-dried overnight at 60 °C. The product was then calcined at 200 °C, producing the ZnO nanomaterials [25,38,39].

The chemical reaction for ZnO synthesis is illustrated in Equations (1) and (2).

$$ZnCl_2(aq) + 2NaOH(aq) \rightarrow Zn(OH)_2(s) + 2NaCl(aq) \quad [1]$$

$$Zn(OH)_2(s) \rightarrow ZnO(s) + H_2O(l) \quad [2]$$

2.2.3. Synthesis of g-C_3N_4/ZnO nanocomposites

The same procedure was used to synthesize the g-C_3N_4/ZnO (GZ) nanocomposites, but g-C_3N_4 was added to the $ZnCl_2$ solution before adding 1.00 mol/L NaOH. $ZnCl_2$(s) (5.00 g) was dissolved in distilled water (50 mL). To achieve thorough dissolution of the $ZnCl_2$, the solution was heated to 80 °C, and 2 to 3 drops of HCl (32 %) were added. g-C_3N_4 nanosheets (5.00g) were added to the solution and agitated to form a homogeneous suspension. Then, 1.00 mol/L NaOH was added to the rest and stirred for 2 h. The reaction was kept at a pH range of 9–11. The g-C_3N_4/ZnO nanomaterials that were produced were centrifuged, cleaned with distilled water, and left to dry at 60 °C overnight in the oven [31].

2.2.4. Synthesis of silver oxide (Ag_2O) nanoparticles

The chemical precipitation procedure was used to synthesize Ag_2O nanoparticles; this is illustrated in Equation (3). $AgNO_3$ (5.00 g) was dissolved in distilled water (50.0 mL). Thereafter, the mixture was agitated magnetically for 30 min. Then, a dropwise addition of aqueous NaOH solution (1.00 mol/L, 40.0 mL) produced a dark brown silver oxide precipitate. Stirring was continued for an additional 30 min to allow a complete reaction. The dark brown silver oxide nanoparticles were recovered after centrifuging and washing multiple times with distilled water. This was undertaken to dissolve the by-products, such as sodium nitrate. The product was then washed with ethanol to hasten the drying process of the silver nanoparticles. The produced nanoparticles were left to dry overnight in an oven set at 60 °C [28].

$$2AgNO_3\ (aq) + 2NaOH\ (aq) \rightarrow Ag_2O\ (s) + 2NaNO_3\ (aq) + H_2O \quad [3]$$

2.2.5. Synthesis of g-C_3N_4/Ag_2O nanocomposites

The nanocomposites of g-C_3N_4/Ag_2O (GA) were synthesized using the same approach as the synthesis of Ag_2O. In contrast, g-C_3N_4 nanosheets were introduced into the $AgNO_3$ solution before adding NaOH to the reaction. Distilled water was used to suspend g-C_3N_4 (5.00 g) and was sonicated for 30 min to ensure homogenous dispensation. After that, $AgNO_3$ (5.00 g) was added, and the suspension was magnetically agitated for 30 min to allow for complete dissolution. After that, 1.00 mol/L NaOH (40 mL) was added dropwise to the mixture. The NaOH served as a reducing agent to help adjust the pH of the solution to a basic range, which was required to form silver oxide nanoparticles. The basic solution stabilized the nanoparticles and prevented them from agglomerating or clumping together. After adding the aqueous NaOH, a dark brown suspension was produced. The suspension was stirred for 30 min to ensure the complete reaction. Later, the mixture was centrifuged and washed with distilled water and ethanol and dried at 60 °C overnight; the g-C_3N_4/Ag_2O nanocomposites were obtained [31].

2.2.6. Synthesis of g-C_3N_4/ZnO/Ag_2O nanocomposites

The g-C_3N_4/ZnO/Ag_2O (GZA) nanocomposites were produced using a hydrothermal process. Distilled water (50 mL) was used to suspend g-C_3N_4 (3.00 g) while stirring. Then, $AgNO_3$ (1.50 g) and zinc acetate (1.50 g) were introduced into the system. The liquid was agitated for 1 h to dissolve the salts completely; after that, 1.00 mol/L of NaOH was added while stirring. The mixture was then transferred into a Teflon autoclave and placed in a 120 °C oven for 12 h. The g-C_3N_4/ZnO/Ag_2O nanocomposites were then washed with distilled water and dried at 60 °C in an oven [31].

2.2.7. Synthesis of carrageenan nanocomposites

In a 100 ml round bottom flask, 1.00 g of κ-carrageenan (Carr) of food grade was dissolved in 50 mL distilled water at 80 °C. 1.00 g of the different nanomaterials was added to the reaction mixture to obtain the respective nanomaterial/carrageenan nanocomposite. The mixture was kept under magnetic stirring for 30 min at 80 °C. The mixture was then placed in an oven at 60 °C for 4 h to evaporate the water [40]. The prepared nanocomposites were designated as g-C_3N_4_Carr, ZnO_Carr, GZ_Carr, Ag_2O_Carr, GA_Carr, GZA_Carr.

2.3. Photocatalysis and recyclability analysis

A 300 W xenon lamp served as the visible light source to induce the photocatalytic reaction of the photocatalysts. 20 mg of the prepared photocatalyst were dispersed in 50 mL of dye solutions with a concentration of 20 mg/L at pH 7. The experiment was conducted in a dark room for 30 min under vigorous stirring to achieve adsorption-desorption stability. During visible light exposure, samples were withdrawn at regular intervals and centrifuged to remove the photocatalysts. Subsequently, the UV–vis spectra of dyes were recorded at their maximum absorption wavelength. The efficiency of the photocatalyst was assessed using the formula $\eta = C/Co$ x 100 %, where C and Co represent the concentrations of the solutions before and after exposure to visible light, respectively.

The recyclability of GZA_Carr was done the same way as the photocatalysis. Since the GZA_Carr nanocomposites showed a higher degradation rate compared to the other nanocomposites, they were selected and used for recyclability. In this case, the photocatalysts were washed several times with deionized water, centrifuged, and dried before being reused for photocatalysis [2,41,42].

2.4. Characterization of nanomaterials and nanocomposites

2.4.1. Fourier transform infrared spectroscopy (FTIR)

Following synthesis, the composition of the produced nanomaterials was confirmed using a Fourier transform infrared) (FTIR) spectrometer (PerkinElmer, Spectrum 100, Made in Liasntrisant, United Kingdom). The measurement was taken in the 3500-400 cm^{-1} range. Before analysis, the samples were ground into a fine powder and mixed with potassium bromide (KBr). The KBr acts as a diluent or matrix, analyzing the sample as a solid rather than a liquid. It also helps to reduce water absorption and other impurities in the sample, which can interfere with the analysis.

2.4.2. X-ray diffraction Spectroscopic analysis

X-ray diffraction (XRD) spectrometric analysis was used to measure the crystallinity of the nanomaterials. The powdered samples were carefully loaded into metal sample holders. The PANalytical XPERT-PRO Diffractometer, manufactured by Panalytical in Malvern, UK, was used to conduct the analysis using CU Kα ($\lambda = 1.54$) between 2Θ values 2–90°.

2.4.3. Scanning electron Microscopic analysis

The surface morphology of the modified nanomaterials and nanocomposites was examined using a VEGA3 TESCAN scanning electron microscope (SEM) manufactured in Brno, Czech Republic. Before characterization, the samples were mounted on a sample holder on carbon tape. To improve their imaging, the samples were coated with a thin layer of conductive material (carbon). The coating helps to prevent charging effects and improves image resolution. While imaging, a beam intensity of 12 kV, at HV of 20 kV, and a secondary electron (SE) detector were used.

2.4.4. Transmission electron Microscopic analysis

The morphology and size of the produced nanocomposites were investigated using transmission electron microscope (TEM) analysis. The TEM analyses were conducted on a Jeol JEM-2100F transmission electron microscope machine equipped with a LaB6 source from Jeol (Tokyo, Japan) at an acceleration voltage of 200 kV. The synthesized nanomaterials were dropped individually on a 200-mesh Cu-grid coated with a carbon film to prepare the TEM samples. Ethanol was used as a dispersant. The images of the nanocomposites were captured using a digital charge-coupled device camera connected to the transmission electron microscope.

2.4.5. Ultraviolet–Visible spectrophotometer

The photocatalysis efficiency was measured using the Shimadzu UV-2450 Ultraviolet–Visible spectrophotometer (UV–Vis). The ultraviolet diffuse reflectance spectroscopy (UV DRS) was conducted using the Evolution Pro, Model 840–340200, UV–Vis

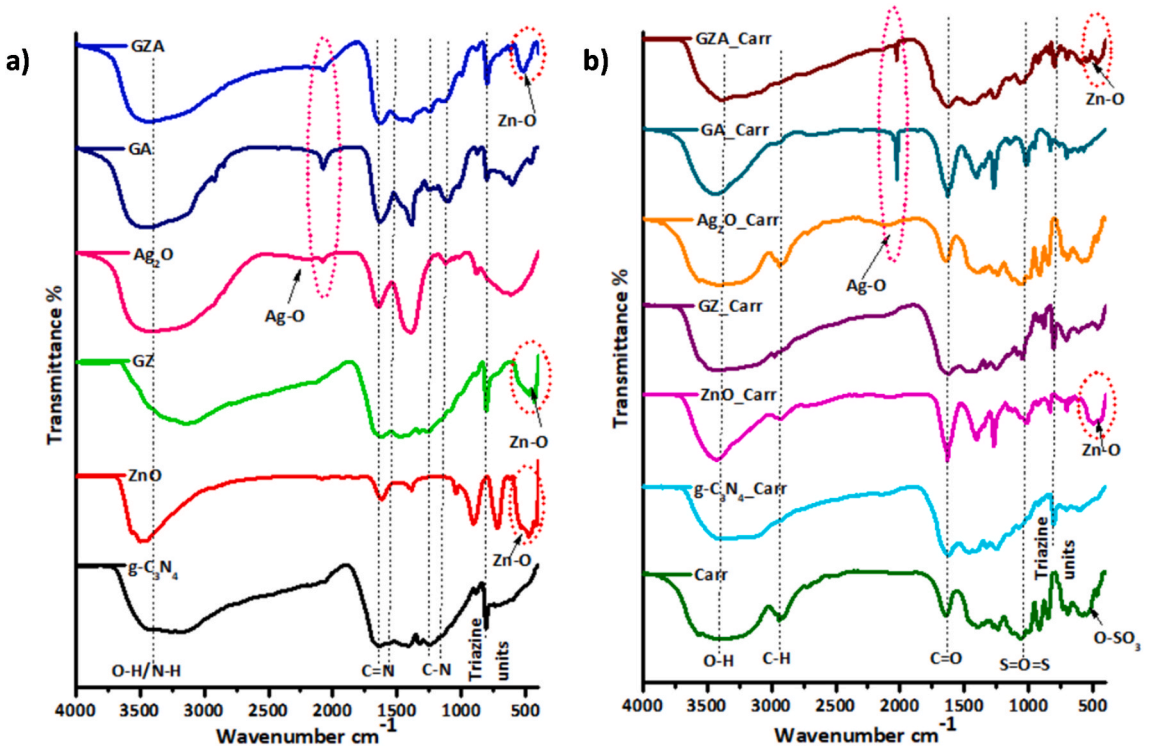

Fig. 1. (a) FTIR spectrum of synthesized g-C_3N_4 nanosheets, ZnO, Ag_2O and nanocomposites (b) carrageenan and their nanocomposites.

spectrophotometer containing a Xenon lamp. $BaSO_4$ was used as a reference material to determine the band gap of nanomaterials.

2.4.6. Photoluminescence

The optical properties of the nanomaterials were determined using the Shimadzu RF-6000 fluorescence spectrofluorophotometer in Kyoto, Japan. The samples were dispersed in distilled water and sonicated for 30 min before analysis.

2.4.7. Zetasizer

The zeta potential of all nanomaterials was determined by the Zetasizer Zen3600, manufactured by Malvern Instruments Limited in Worcestershire, United Kingdom. The samples were dispersed in water at a 1mg/100 mL concentration. The dispensation was then sonicated for 30 min to ensure proper dispersion. The pH of the samples was adjusted with NaOH and HCl.

3. Results and discussion

3.1. Chemical composition of nanomaterials

FTIR was used to ascertain the functionality of the nanomaterials and carrageenan and its nanocomposites, as shown in Fig. 1. A broad peak (3500 cm^{-1} and 2700 cm^{-1}) denoted the N–H stretching of the g-C_3N_4, indicating the successful conversion of melamine into g-C_3N_4 nanomaterials [24,43]. On the other hand, the C–N and C═N heterocyclic ring stretching was observed at 1850-1000 cm^{-1}, confirming the successful formation of the g-C_3N_4. Additionally, the sharp peak observed at 810 cm^{-1} was due to the s-triazine breathing mode or the heptazine's out-of-plane collective wagging mode of the N and C atoms [24,35,44,45]. These C–N, C═N stretches, and triazine units were observed throughout the nanocomposites synthesized after that. This was confirming the successful preparation of the nanocomposites. Moreover, the vibrational frequencies are unaffected by small changes in the molecule's environment or modification of the g-C_3N_4 material.

After incorporating Ag_2O nanomaterials onto g-C_3N_4, a sharp peak at 2072 cm^{-1} was observed. This peak was attributed to the Ag–O stretching bond on the GZA nanocomposites and the GZA_Carr nanocomposites thereof. The g-C_3N_4 characteristic peaks are maintained, as mentioned earlier, demonstrating a minimal disturbance and confirming the coexistence of g-C_3N_4, Ag_2O and ZnO in the nanocomposites' matrix. Similarly, the Zn–O stretching vibration was observed at 590-404 cm^{-1} [45]. The appearance of the Ag–O and Zn–O functional groups for the GZA nanocomposites indicated that the Ag_2O and ZnO were successfully incorporated onto the surface of g-C_3N_4 nanosheets [46].

The functionalities of the carrageenan sulfate esters (S═O═S, O–SO_3) were observed at 1210-1260 cm^{-1} region (due to the S═O of sulfate esters). The O–SO_3 group is observed at 460–567 cm^{-1}. The 1010-1080 cm^{-1} region was ascribed to glycosidic linkage found

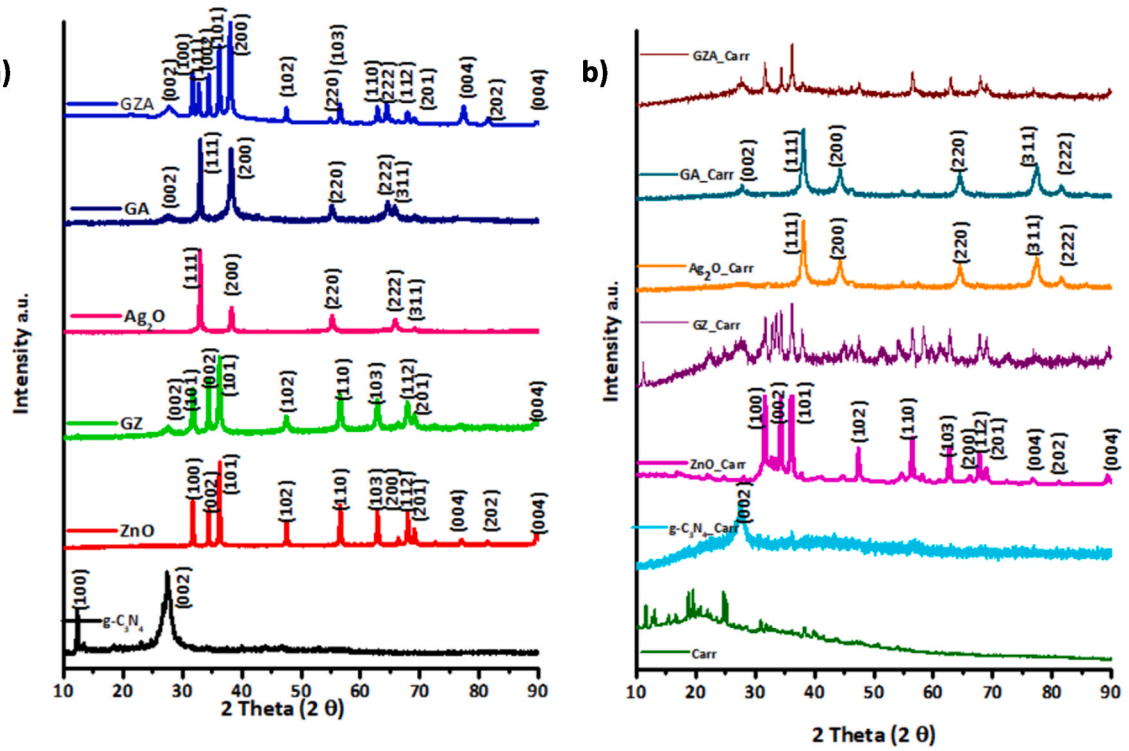

Fig. 2. (a) XRD patterns of Ag_2O, ZnO, g-C_3N_4 and composites, and (b) carrageenan nanocomposites.

within the carrageenan structure. Consequently, all carrageenan nanocomposites had a particularly strong signal at 803-905 cm^{-1}, which was specific to 3,6-anhydrogalactose-2-sulfate and D-galactose-4-sulfate characteristic of carrageenan [47,48]. The FTIR spectra of the control carrageenan nanocomposites showed similar patterns in the positions of characteristic bands, indicating that carrageenan had good miscibility with nanocomposites. However, there was an overlap of the carrageenan and g-C_3N_4 peaks on the nanocomposites.

An XRD spectroscopy was used to identify the crystal shape of the g-C3N4, ZnO, and Ag2O nanomaterials and the changes occurring after nanocomposite preparation and carrageenan. This is illustrated in Fig. 2. Characteristic diffraction patterns of g-C_3N_4 were observed at 2θ values of 12° and 27° assigned to 100 and 002 lattice planes, respectively, as reported by Alaghmandfard [24] and

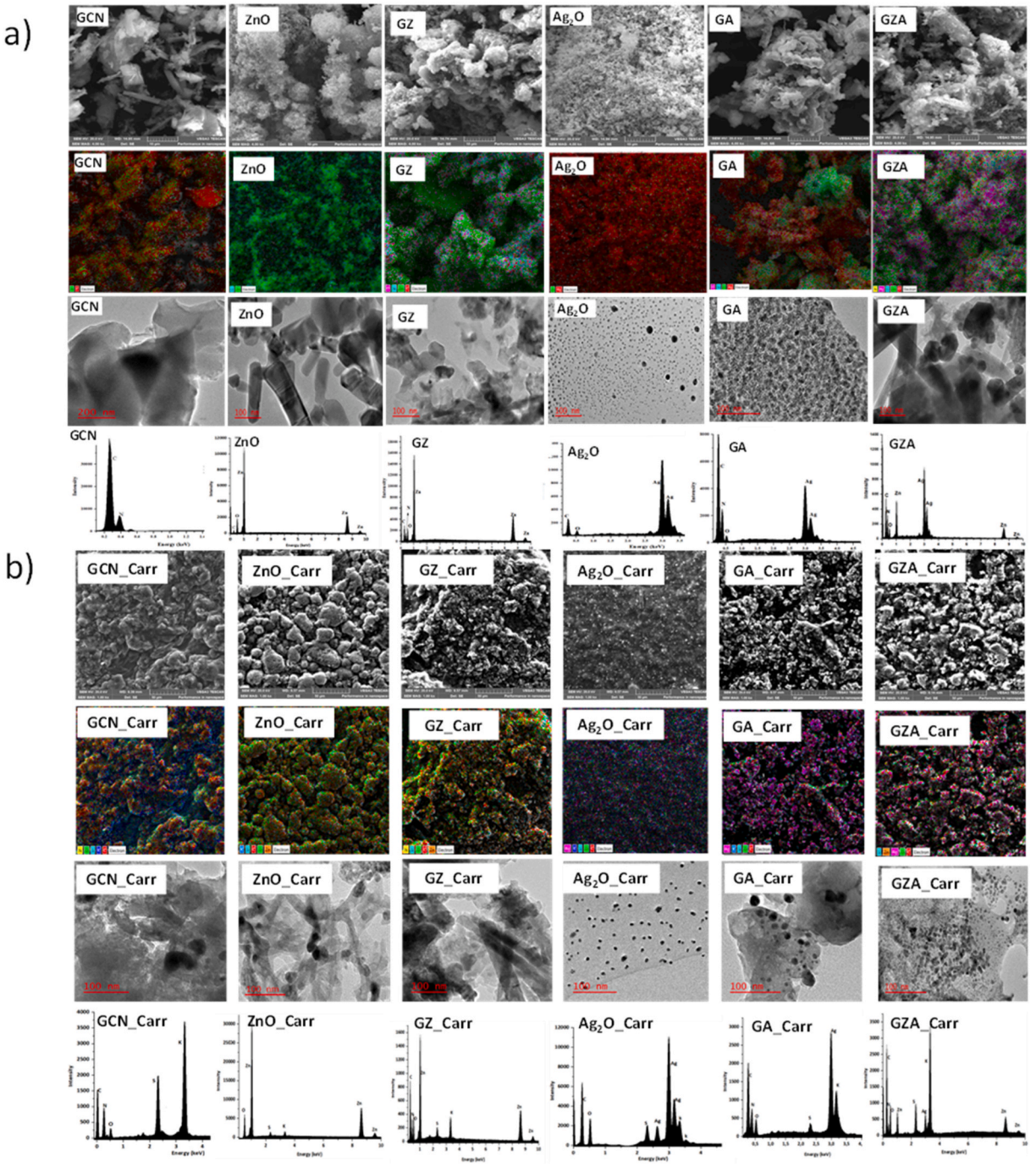

Fig. 3. SEM and TEM micrographs and SEM-EDX/mapping for a) g-C_3N_4, ZnO, GZ, GZA and b) carrageenan nanocomposites.

Paul et al. [49]. This corresponded to the interlayer stacking of the conjugated carbocyclic plane of the tri-*s*-triazine unit. Ag_2O peaks at 32.99°, 38.28°, 55.28°, and 65.98° corresponded to the crystal plane of the cubic Ag_2O [30,50,51]. The hexagonal planar of the pure ZnO was observed at 31.63°, 34.16°, 47.55°, 56.64°, 63.17°, 67.84°, and 69.07° [28]. The well-defined peaks in Fig. 2a indicated the high crystallinity of the nanomaterials and nanocomposites as opposed to the peaks in Fig. 2b [52].

In all nanocomposites, the g-C_3N_4 was represented by the diffraction peaks at about 27°, confirming the incorporation/embedded onto the g-C_3N_4 [22,53,54]. New peaks arising from the addition of the ZnO and Ag_2O nanoparticles onto the g-C_3N_4 were also observed among the resultant nanocomposites. For example, the GZ, GA, and GZA nanocomposites exhibited peaks with positions resembling those of the g-C_3N_4, ZnO, and Ag_2O as determined by XRD analysis. Furthermore, the peaks of the GZ nanocomposites were observed at 27.57°, 31.72°, 34.50°, 36.26°, 47.71°, 56.54°, 62.72°, 66.24°, 68.00°, 69.01°, and 76.83° whereas the peaks of the GA nanocomposites were at 27.69°, 32.99°, 38.16°, 44.45°, 55.16°, 64.60°, and 77.58° [2,55].

The GZA structure revealed the presence of Zn, C, N, O, and Ag nanomaterials, as reported in the literature [21,25,31,32]. This indicated that the lattice structure of the nanomaterials remained unaltered upon combining g-C_3N_4 with the metal oxides, as shown in the FTIR analysis. The lattice structure of nanomaterials plays a crucial role in determining their electronic and optical properties, which in turn influence the photocatalytic activity of the resultant nanocomposites. Therefore, the coexistence of the g-C_3N_4, ZnO, and Ag_2O within the nanocomposite's matrices without significant modification of the original lattice structure of the nanomaterials provided a favourable environment for maintaining and even enhancing their inherent electronic and optical properties, consequently benefiting the photocatalytic activity of the resultant nanocomposites. Thus, it can be assumed that the –C_3N_4, ZnO, and Ag_2O and nanocomposites will be able to absorb light [56–58].

The incorporation of nanomaterials and nanocomposites to carrageenan made the resultant nanocomposites slightly amorphous based on the slight broadening of the XRD peaks. This suggested that the interaction between the carrageenan matrix and the nanomaterials disrupted the crystalline structure of the nanomaterials, potentially enhancing their dispersibility within the matrix and favourably influencing their performance in various applications [59,60]. However, the lattice structure of the nanomaterials and nanocomposites remained the same. This demonstrated that the incorporation of the carrageenan was not interfering with the properties of the nanocomposites; instead, it enhanced their effectiveness because of the increased surface area.

The XRD data further provided more insights into the nanomaterials' crystal structure and morphology, enabling a deeper understanding of their properties and environmental interactions. For instance, ZnO suggested a unique arrangement of atoms in a hexagonal planar morphology. The shape of the nanomaterials, especially the hexagonal planar morphology, is known to impact the photocatalytic reactivity properties of the nanoparticles and how the photocatalytic systems interact with other substances within the aqueous media and enable surface adsorption [55,61]. This implied that the incorporation of the nanocomposites into carrageenan would enhance the catalytic properties of the nanomaterials.

On the XRD, there was a slight shift toward the left of the XRD peaks on the nanocomposites. The observed shifts in peak positions indicate that the presence of these materials in the GZA composite or carrageenan nanocomposites influences their crystal structures or lattice parameters. These shifts may be attributed to strain between the components.

3.2. *Morphological properties of nanomaterials (SEM/TEM) and EDX/mapping*

The SEM micrographs and the corresponding energy dispersive spectrometry (EDX) results of g-C_3N_4, ZnO, GZ, Ag_2O, GA, and GZA are shown in Fig. 3a. The SEM micrographs of g-C_3N_4_Carr, ZnO_Carr, GZ_Carr, Ag_2O_Carr, GA_Carr, and GZA_Carr are also illustrated in Fig. 3b. The SEM revealed that the g-C_3N_4 had a stacked layer morphology, whereas the metal oxides were granular. The ZnO and Ag_2O had a granular morphology and powdery texture, whereas the nanocomposites GZ were fluffy, indicating the combination of nanosheets and nanomaterials. When the 3 nanomaterials (g-C_3N_4, ZnO, Ag_2O) were combined, they resulted in the GZA nanocomposites with a stacked layer with granular morphology. The carrageenan nanocomposites had an appearance that looked like the nanocomposites without carrageenan. However, the slight difference was that the surfaces of the nanocomposites modified with the carrageenan had a rough surface topology and cement-like texture. Of note, the GZA_Carr appeared to look like the combination of g-C_3N_4_Carr, ZnO_Carr and Ag_2O_Carr.

SEM-EDX revealed the elements from the nanomaterials, which was consistent with the observations made with the FTIR and XRD results regarding the composition of the nanomaterials and nanocomposites. C, N, Zn, O, and Ag elements were detected from the g-C_3N_4, ZnO, and Ag_2O nanomaterials. Similarly, these elements were also observed from the GZ, GA, GZA, and carrageenan nanocomposites, as illustrated in Fig. 3. Once the nanomaterials and nanocomposites were embedded in carrageenan (Fig. 3b), the EDS spectrum revealed the presence of additional elements, such as carbon (C), sulfur (S) and potassium (k), originating from the carrageenan matrix. The SEM mapping complemented the EDX by demonstrating the elemental composition of the as-obtained samples. It revealed the existence of C and N functionalities in the g-C_3N_4, Zn, O for ZnO, Ag, O for Ag_2O and C, N, O, Ag, Zn for GZA, confirming success in synthesizing nanocomposites. For carrageenan nanocomposites, the S and K elements were observed as a result of the pendant groups of the biopolymer. The elemental analysis of the g-C_3N_4, Ag_2O and ZnO nanomaterials demonstrated an even distribution of the elements of the nanomaterials. The even distribution of the C, N, O, Ag, and Zn on the SEM mapping confirmed an adequate dispersion of these elements through the surfaces of the nanocomposites [46].

TEM analysis was used to examine the morphology of the g-C_3N_4, ZnO, GZ, Ag_2O, GA and GZA nanocomposites to complement the SEM and XRD results. The g-C_3N_4 nanosheets were observed. As predicted by XRD, the hexagonal structure of ZnO and the spherical structure of Ag_2O were also observed under TEM. The TEM confirmed the co-existence of g-C_3N_4, ZnO and Ag_2O, showing that they were supported onto the g-C_3N_4 nanosheets [49,62]. The generated nanomaterials, under 20 nm, exhibited a smaller grain size. This could lead to an increased surface area-to-volume ratio, implying that the nanomaterial's catalytic activity will be significantly

enhanced [29,62]. On the other hand, the carrageenan formed sheets as the nanocomposites were incorporated. The ZnO nanorods were observed clearly on the GZ_Carr, whereas on the ZnO_Carr and GZA_Carr, only the heads of the nanorods were observed.

3.3. Optical properties of nanomaterials (bandgap & photoluminescence)

The results of the UV–Vis absorption spectra were used to determine the band gap energy of each nanomaterial (Fig. 4) using Tauc's equation in Equation (4) for direct band gap material [63–65].

$$(\alpha h\upsilon)^2 = k(h\upsilon - E_g) \tag{4}$$

where, hυ is the photon energy, E_g is the band gap energy, k is a constant, and α is the absorption constant. Equation (4) can be further expressed as:

$$(2.303 \times A \times 1240/\lambda)^2 = k\frac{1240}{\lambda - E_g} \tag{5}$$

where; A and λ are absorbance and wavelength, respectively, obtained from the absorption spectra of the nanomaterials. A plot of Equation (4) gives an absorption curve whose tangent expresses the energy band gap of the nanomaterials. A straight-line curve was extrapolated between (αhυ) and hυ to determine the optical band gap (Fig. 4).

The calculated band gap of g-C_3N_4, ZnO, GZ, Ag_2O, GA, and GZA were 2.80 eV, 3.25 eV, 3.00 eV, 1.63 eV, 1.99 eV and 2.73 eV respectively, as listed in Table 1, and these corresponded to literature values as reported by Sett et al., Hakimi et al., and Paul et al. [45,66,67]. However, the addition of carrageenan did not alter the band gap of the nanomaterials, as the band gaps remained relatively the same. For example, the band gap for g-C_3N_4_Carr, ZnO_Carr, GZ_Carr, Ag_2O_Carr, GA_Carr, and GZA_Carr were 2.79 eV, 3.25 eV, 3.01

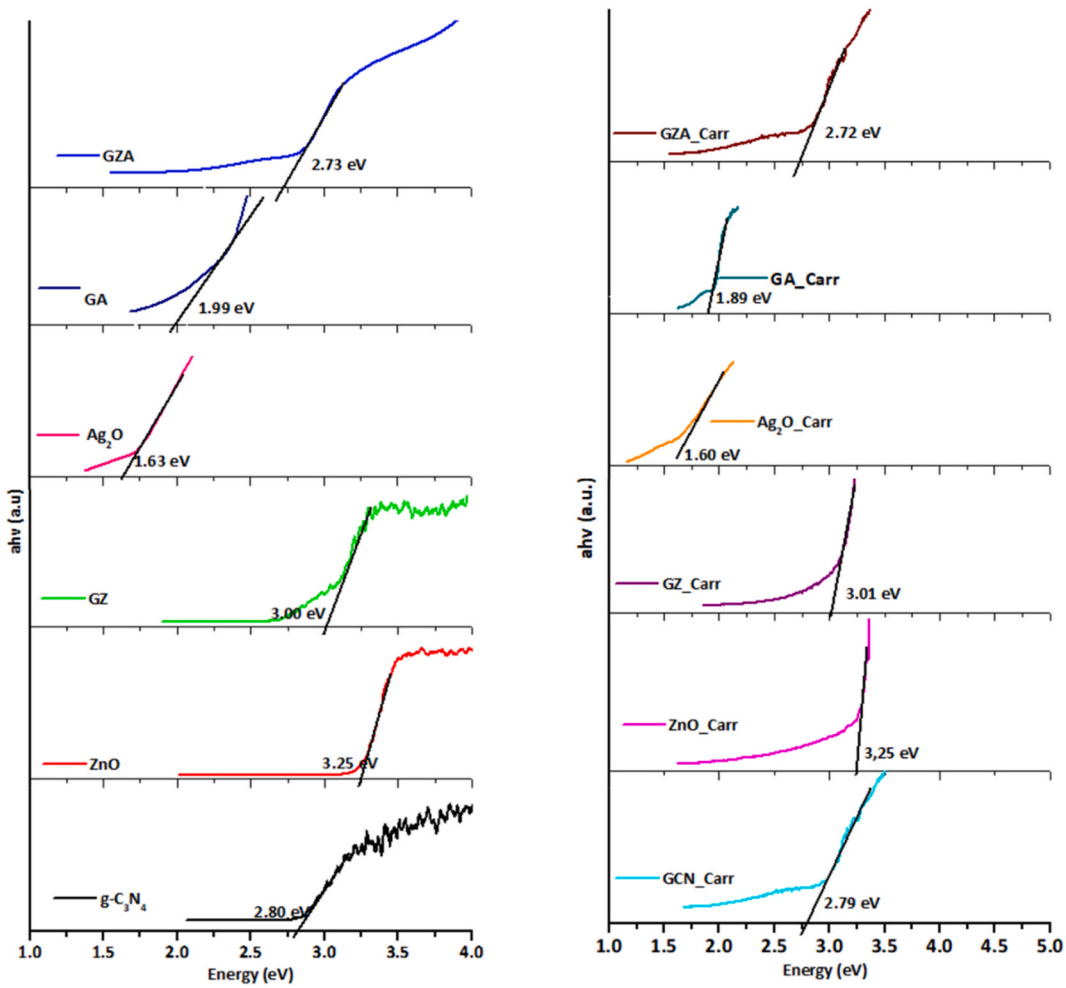

Fig. 4. The energy band gap of different nanomaterials and nanocomposites estimated by the extrapolation of the linear part of $(\alpha h\nu)^2$ versus hν plots.

Table 1
The emission wavelength of nanomaterials after 380 nm excitation and the corresponding band gap.

Nanomaterial	Emission wavelength (nm)	Band gap	Nanomaterial	Emission wavelength (nm)	Band gap
g-C_3N_4	430	2.80	g-C_3N_4_Carr	430	2.79
ZnO	455–706	3.25	ZnO_Carr	425, 418-700	3.25
GZ	460	3.00	GZ_Carr	431	3.01
Ag_2O	432	1.63	Ag_2O_Carr	425	1.60
GA	435	1.99	GA_Carr	436	1.89
GZA	444, 580	2.73	GZA_Carr	433, 557	2.72

eV, 1.60 eV, 1.89 eV, 2.72 eV, respectively. For instance, the band gap for g-C_3N_4 was 2.80 eV, and g-C_3N_4-Carr was found to be 2.79 eV. This implied that the electronic properties of g-C_3N_4-Carr remained relatively consistent with those of pristine g-C_3N_4.

Since the band gap of Ag_2O is small, it influences the band gap of nanocomposites, thus reducing all the Ag_2O-based nanocomposites. The reduced band gap implies that the distance between the valence band of electrons and the conduction band was reduced. A reduced band gap allows nanoparticles to excite electrons within the nanocomposites with minimal energy input, promoting their transition to the conduction band. This lowered energy requirement enhances the nanocomposite's capacity to facilitate electron conduction. Consequently, the preparation of these nanocomposites results in an enhancement of their photocatalytic properties [63–65].

Fig. 5a shows PL emission spectra of pure g-C_3N_4, ZnO, GZ, and GZA observed after the excitation of samples at the visible region at 380 nm at room temperature. Fig. 5b also shows the photoluminescence of carrageenan nanocomposites, which showed lower emission intensities than those without carrageenan. The pure g-C_3N_4 sample exhibited an intense fluorescence emission peak at 430 nm. However, the ZnO (455–706 nm), GZ (460), Ag_2O (432), GA (435) and GZA (444, 580 nm) showed lower photoluminescence intensity than the pure g-C_3N_4. The emission peak intensity of the nanocomposites was drastically reduced as the metal oxide nanomaterials were combined with g-C_3N_4 nanosheets [29,31,68].

The pure g-C_3N_4 sample exhibited a strong fluorescence emission peak at a wavelength of 430 nm. This means that when pure g-C_3N_4 was exposed to light, it emitted a significant amount of fluorescence at this specific wavelength, indicating its photoluminescent behavior. In contrast, when ZnO and Ag_2O were combined with g-C_3N_4 to form nanocomposites (GZ, GA, GZA), the photoluminescence intensity decreased. This means that the nanocomposites emitted less fluorescence compared to pure g-C_3N_4. It was also suggested that the electrons and holes do not recombine quickly but are instead available for catalytic reactions [54,69].

The emission peak of GZA nanocomposites has moved to the right at a higher wavelength when compared to pure ZnO and Ag_2O, which implies that the band gap was reduced as the narrow band gap Ag_2O was added. In addition, the peak intensity for GZA decreased, implying that the recombination of the photoexcited electron and a hole may be inhibited, leading to better photocatalytic performance. When light interacts with nanomaterials, pairs of electrons and holes are produced. These separated charge carriers are essential for photocatalysis, as they participate in chemical reactions. However, if these electrons and holes recombine quickly, their potential for driving photocatalytic reactions is wasted. The introduction of g-C_3N_4, ZnO, and Ag_2O into the nanocomposites seems to inhibit this recombination process. In other words, these materials help keep the electrons and holes separated for longer periods [70,71].

Therefore, GZA was expected to have a better opportunity to enhance the photocatalytic performance. This was because, during photocatalysis, the electrons from the valence band of g-C_3N_4 were transferred into the conduction band through the synergistic system during excitation. Since the g-C_3N_4, ZnO, and Ag_2O have different band edge potential levels, the electrons from the g-C_3N_4 conduction band are transferred to the conduction band of the ZnO and Ag_2O nanoparticles at varied rates and distances. Then, the holes in the

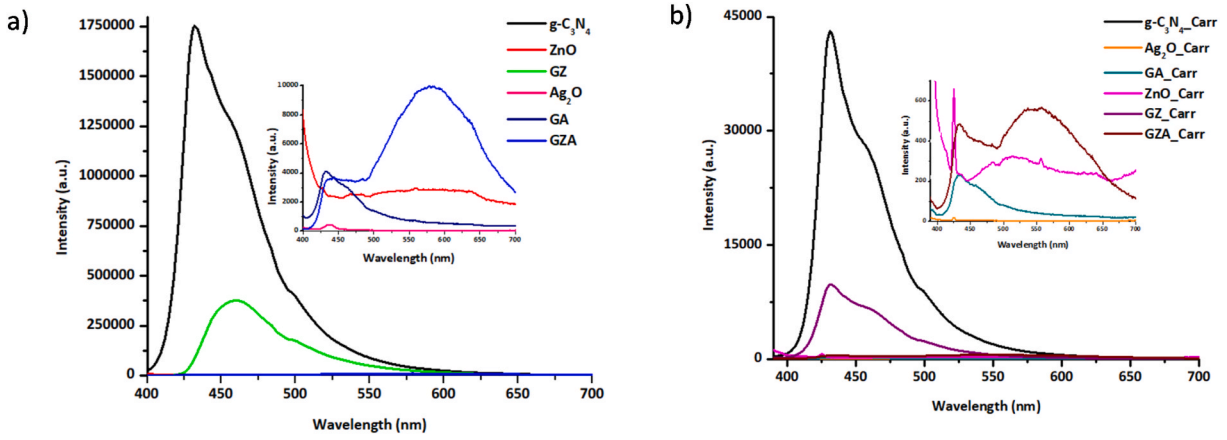

Fig. 5. PL spectra for a) g-C_3N_4, ZnO (inset), GZ, Ag_2O, GA and GZA (inset) and b) g-C_3N_4-Carr, ZnO_Carr (inset), GZ_ Carr, Ag_2O_Carr, GA_ Carr and GZA_Carr (inset) at 380 nm excitation.

ZnO and Ag_2O were easily transferred to the valence band gap of g-C_3N_4, thereby enabling/facilitating a better transfer of electrons from the valence band to the conduction band [2,68].

The PL wavelength of carrageenan-based nanocomposites shifted towards the left, leaning toward the UV range. However, the emission is still in the visible region (400–800 nm). The photocatalysts had an emission peak of more than 400 nm; thus, they can be used for visible light photocatalysis. So, the photocatalysts with an emission peak of more than 400 nm can be excited by photons with wavelengths in the visible light range [72,73]. The slight shift in the photoluminescence (PL) wavelength of carrageenan-based nanocomposites towards the UV range can be attributed to the interaction between carrageenan and the nanomaterials within the composites. Although not a major shift, this phenomenon indicates subtle changes in the electronic structure and environment of the nanomaterials when combined with carrageenan. Here's how carrageenan might be causing this slight shift. Carrageenan is a biopolymer with unique chemical properties. When it is incorporated into nanocomposites, it can introduce modifications to the electronic environment around the nanomaterials. This can result in small changes in the energy levels associated with photoluminescence processes, leading to a shift in the PL wavelength [72,73].

Photocatalysts with emission peaks in the blue (440–490 nm) and green (490–570 nm) regions of the visible light spectrum are often more efficient than photocatalysts with emission peaks in the red region. This is because photons with shorter wavelengths have more energy and can excite more electrons in the photocatalyst. Of note, the ZnO_Carr had two distinct emission peaks. One visible emission appeared at 425 nm (sharp), and another was a broad peak between 450 and 700 nm with a maximum located at 510 nm due to oxygen vacancies of ZnO nanomaterial [74–76]. The peak at 425 nm is due to the recombination of the free excitons through an exciton–exciton collision process [75,76]. The PL intensities of carrageenan-doped nanocomposites were lesser than those of nanomaterials without carrageenan. This demonstrated that doped nanocomposites had an advancement in their optical properties. This is attributed to the fact that the doped ions offer various electron traps to hinder electron-hole pairs' recombination [76].

3.4. Zeta potential of nanomaterials and nanocomposites

Photocatalysis takes place on the surface of the nanomaterials, and the surface capacity to adsorb the pollutant and the solution pH has a significant impact on the photocatalyst's performance. The charge on the surface of the synthesized nanomaterials and the point of zero charge (PZC) were determined [77]. From Fig. 6, it was noted that g-C_3N_4 nanosheets and carrageenan surfaces are charged negatively at all pH values. This is so because g-C_3N_4 contains negatively charged functional groups, such as amine (NH) groups [78], while carrageenan contains ester hydroxyls, sulfates and 3,6-anhydro-D-galactose [47,48]. The PZC of the ZnO, GZ, Ag_2O, GA, and GZA nanocomposite were 6.00, 4.67, 2.49, 2.18, and 2.97, respectively. However, the PZC for ZnO_Carr, GZ_Carr, Ag_2O_Carr, GA_Carr and GZA_Carr nanocomposite was 5.84, 4.45, 2.26, 2.13, and 2.82, respectively. Since carrageenan is highly negatively charged at all pHs, the PZC of the carrageenan nanocomposites shifted towards the left. The nanomaterial's surface is negatively charged at pH > PZC and positively charged at pH < PZC. Fig. 6 shows that nanomaterials had more negative charges as the pH increased [30,77,79]. The change in surface charge is due to protonation and deprotonation; thus, the adsorbent can effectively adsorb the cationic contaminant when the pH of solutions is greater than PZC and vice versa [79].

The introduction of g-C_3N_4 influenced the surface properties of nanocomposites, shifting the PZC to a lower pH value. For example, the point of zero charge of ZnO moved from pH 6.00 to 4.67 when the g-C_3N_4 nanosheets were introduced. Similarly, the PZC of Ag_2O is 2.49, and for GA, the PZC shifted lightly to pH 2.18. This is because when g-C_3N_4 is introduced to form a nanocomposite with ZnO or Ag_2O, it interacts with ZnO or Ag_2O through electrostatic interactions, hydrogen bonding, and van der Waals forces. These interactions can lead to forming a new surface with different charges and properties compared to the original g-C_3N_4, ZnO, or Ag_2O surface. At pH values above the PZC, the surfaces of metal oxides are negatively charged due to the adsorption of hydroxide ions (OH^-) from the solution and positively charged due to the adsorption of protons (H^+) from the solution.

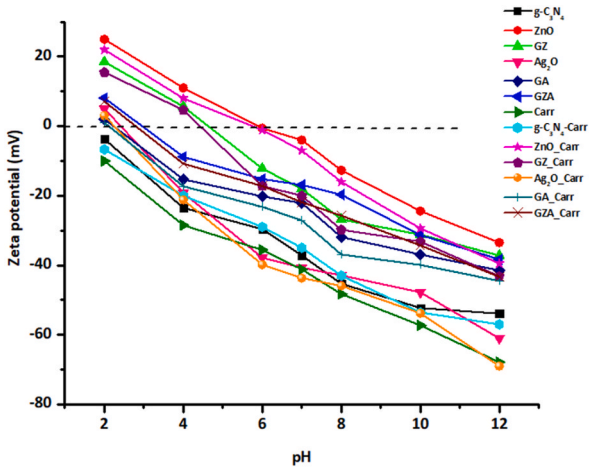

Fig. 6. Zeta potential of g-C_3N_4, ZnO and GZA and carrageenan nanocomposites.

3.5. Photocatalytic studies for cationic and Anionic dyes

The photocatalytic performance of nanomaterials was assessed under visible light irradiation to remove methylene blue (MB), methyl violet (MV), methylene green (MG) and Congo red (CR) dyes from the solution. The dye solution was set at 20 ppm, and a 20 mg catalyst dosage was used. To ensure the solution had reached the adsorption-desorption equilibrium before irradiation, the solution was left in the dark for 30 min. After that, the visible light was turned on for 180 min, and aliquots were taken out of the solution after every 30 min. A PVDF syringe filter (0.22 μm) was used to separate the dye solution and nanomaterials. Degradation efficiency was obtained by the following equation:

$$\text{Degradation } \% = \frac{C_t}{C_0} x\ 100\% \quad [6]$$

where C_o represents the initial dye concentration, and C_t represents the dye concentration after time t [46].

3.5.1. Degradation of Congo red

At the start of the experiment (time = 0), the dye concentration is 100 %. Considering g-C_3N_4, as time progressed, the dye concentration in the solution decreased in the first 30 min, indicating that the dye was being adsorbed. This reduction in dye concentration is reflected in the decreasing percentages in Fig. 7a. After 30 min of adsorption, 1.87 % was adsorbed by g-C_3N_4. Similarly, 2.88 %, 5.10 %, 9.12 %, 38.39 %, 20.36 %, 16.77 %, 8.12 %, 12.95 %, 10.89 %, 3.08 %, 27.8 % were adsorbed by ZnO, GZ, Ag_2O, GA, GZA, g-C_3N_4_Carr, ZnO_Carr, GZ_Carr, Ag_2O_Carr, GA_Carr, and GZA_Carr.

After 30–60 min, there was a gradual decrease in dye concentration. Still, the rate of degradation seems to be relatively slow with g-C_3N_4 compared to GZA_Carr, which had a higher overall degradation rate with a pseudo 1st order and pseudo 2nd order rate constant of 0.0107 min^{-1}, 0.1446 $M^{-1}min^{-1}$ respectively. The dye concentration remains above 88 % for g-C_3N_4 even after 60 min of photocatalysis. However, after 90 min, there's a more noticeable drop in dye concentration, down to 80.67 %. This suggested that the photocatalytic degradation process became more efficient over time until the dye concentration reached 60.44 % at 210 min, indicating that the catalyst remained active for a longer period, leading to enhanced efficiency over time.

GZA and GZA_Carr showed a high adsorption and degradation activity of Congo red, indicating that the preparation of

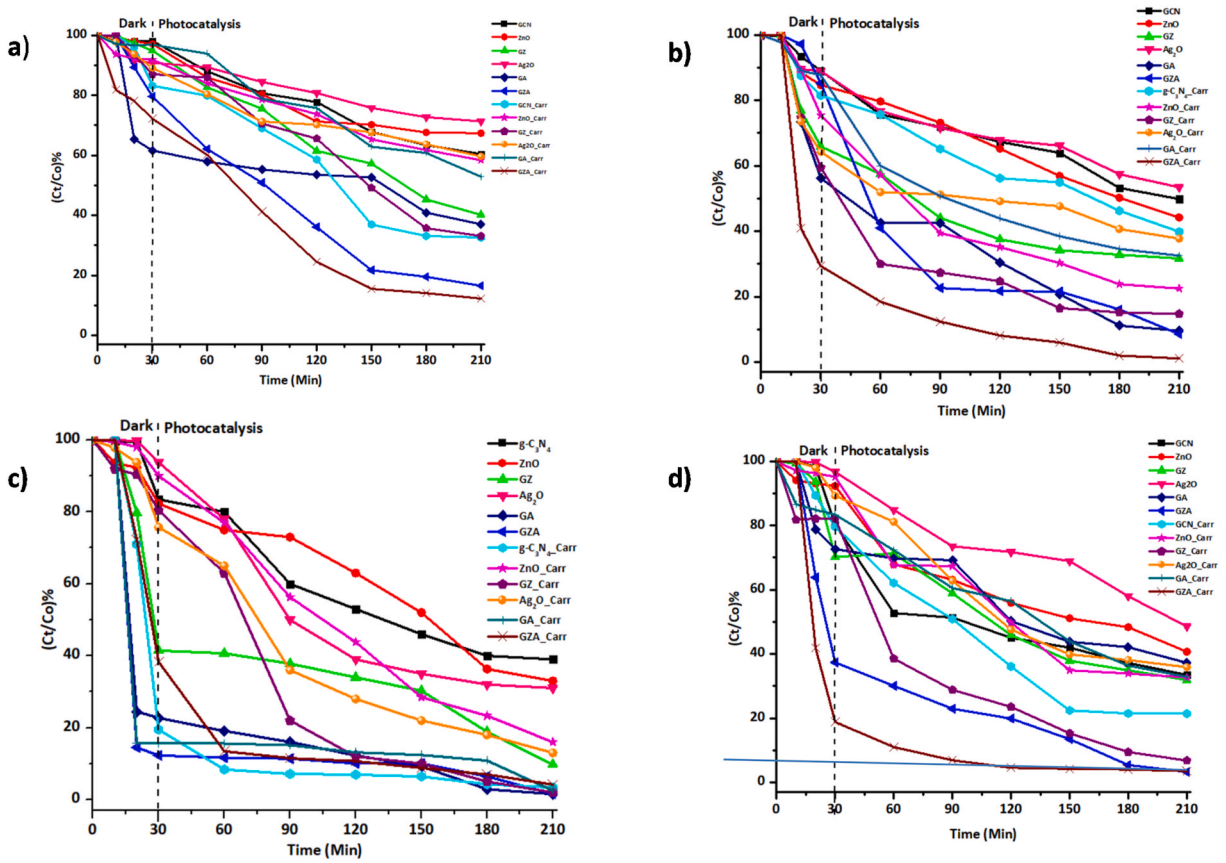

Fig. 7. Photocatalytic degradation of a) CR, b) MV, c) MB, d) MG under visible light by g-C_3N_4, ZnO, Ag_2O, GA, GZ, GZA and carrageenan nanocomposites photocatalysts.

nanocomposites improved the adsorption and photocatalytic efficiency of the nanomaterial. After the entire photocatalysis, g-C_3N_4., ZnO, GZ, Ag_2O, GA, GZA, g-C_3N_4_Carr, ZnO_Carr, GZ_Carr, Ag_2O_Carr, GA_Carr, and GZA_Carr had 39.56 %, 32.62 %, 59.87 %, 28.65 %, 63.00 %, 83.49 %, 67.3 8 %, 41.62 %, 66.90 %, 40.32 %, 47.10 %, 87.76 %. From these results, it is depicted that the degradation of CR was improved when nanocomposites were used. Adding Ag_2O nanoparticles into the GZ nanocomposite improved the photocatalysis of the nanocomposites. For instance, in the GZA nanocomposites, the excited electrons in the CB of ZnO were transported into the CB of g-C_3N_4 and then of Ag_2O by visible light. Also, the holes were moved to the VB of ZnO and g-C_3N_4 from the VB of Ag_2O. This heterogeneous coupling separates charge carriers from junctions, allowing CR to be effectively degraded [68,80,81].

The degradation with GA, GZ, and GZA yielded a greater degradation efficiency, with GZA having a 43.93 % better degradation than that of g-C_3N_4. Of note, adding carrageenan to form nanocomposites also improved the photocatalysis. The carrageenan, as an adsorbent, adsorbed the dye, which leads to better adsorption. Carrageenan also helps disperse the nanocomposites and nanoparticles more uniformly, enhancing their surface area and improving contact with the pollutants, thus leading to increased degradation. In summary, the preparation of nanocomposites has enhanced the degradation of CR.

3.5.2. Degradation of methyl violet

After adsorption at 30 min, 10.91 % was adsorbed by g-C_3N_4. Whereas 15.29 %, 34.11 %, 11.03 %, 33.78 %, 14.72 %, 18.53 %, 24.56 %, 40.51 %, 35.73 %, 12.25 %, 70.64 % was adsorbed by ZnO, GZ, Ag_2O, GA, GZA, g-C_3N_4_Carr, ZnO_Carr, GZ_Carr, Ag_2O_Carr, GA_Carr, and GZA_Carr as shown in Fig. 8b. After that, photocatalysis resumed as the visible light was illuminated. For g-C_3N_4, ZnO, and Ag2O, the photocatalysis was gradual until it reached 50.15 %, 55.80 %, and 46.54 % degradation after 210 min. After 210 min, 68.35 %, 53.02 %, 91.48 %, 60.15 %, 77.55 %, 85.29 %, 62.27 %, 67.50 %, 98.93 % of MV are degraded by GZ, GA, GZA, g-C_3N_4_Carr, ZnO_Carr, GZ_Carr, Ag_2O_Carr, GA_Carr, GZA_Carr. The nanomaterials with higher degradation efficiencies are GZA_Carr, at 98.93 %, and Ag_2O, with a low degradation efficiency of 46.54 % at 210 min. After 180 of illumination, around 1.07 % of MV remained in solution, showing a 98.93 % degradation efficiency of GZA_Carr, which is more efficient than GZA, which had a 91.48 %. This shows that degradation became more effective amongst nanocomposites.

The GZA nanocomposite achieves better dye degradation than pure nanoparticles, as illustrated in Fig. 7 (b). The dye concentration dropped from 100 % to 85.28 % during adsorption, showing a 14.72 % adsorption and obtaining a 91.4 efficiency at 210 min. The addition of Ag_2O accelerates the degradation of the dye. In addition, the g-C_3N_4 and ZnO conduction bands receive electrons from Ag_2O. Ag_2O's valence band serves as a hole centre, while the conduction bands of g-C_3N_4 and ZnO work as electron centres. Reactive

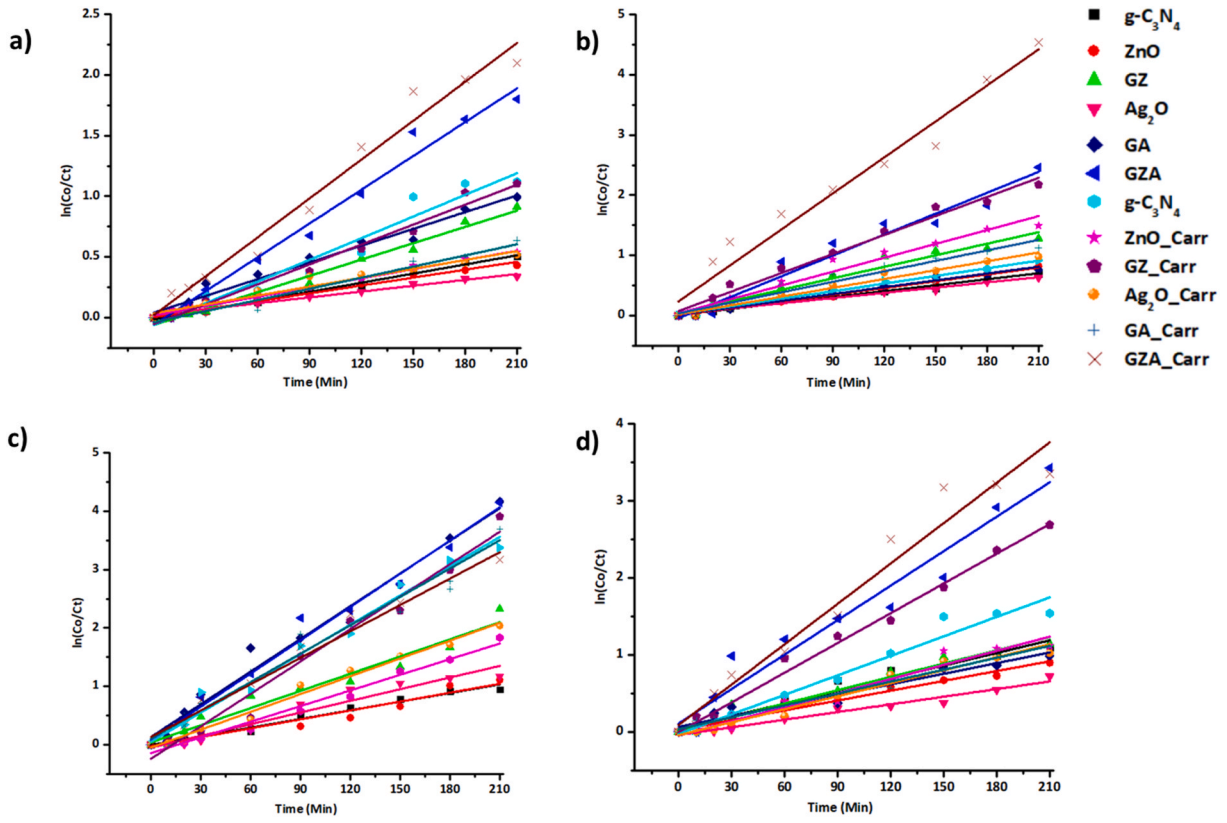

Fig. 8. Pseudo-1st-order rate kinetics for photocatalytic degradation of a) Congo red, b) methylene violet, c) methylene blue, and d) methylene green using the synthesized nanomaterials and nanocomposites.

species are created when oxygen and water molecules react with the electrons and holes from g-C_3N_4 and ZnO and the holes from Ag_2O, leading to dye degradation. The enhanced mobility of charge carriers brought on by Ag_2O's electron trap may have contributed to the GZA nanocomposite's improved photocatalytic activity [30].

3.5.3. Degradation of methylene blue

The degradation performance of nanoparticles and nanocomposites on MB is illustrated in Fig. 7 (c). As time progresses, the concentration of MB decreases as the different photocatalysts facilitate dye degradation. In some cases, the addition of carrageenan seems to enhance the degradation efficiency of certain photocatalysts (e.g., ZnO_Carr and GZ_Carr), while in other cases, it appears to hinder the efficiency (e.g., GA_Carr and GZA_Carr). This suggests that carrageenan's impact on photocatalysis is catalyst-dependent in MB solution. GA_Carr and GZA_Carr display large fluctuations in degradation efficiency over time. Over longer periods, some photocatalysts start to plateau in their degradation efficiency but maintain a high photocatalytic efficiency. The nanomaterials with higher degradation efficiencies are GA, GZA, g-C_3N_4_Carr, GZ_Carr, GA_Carr, and GZA_Carr, at 98.44 %, 98.45 %, 98.42 %, 96.58 %, 98 %, 97.50, 95.82 %, with g-C_3N_4 and ZnO with lowest degradation efficiency of above 60 % after 210 min.

The presence of negative charge on the surfaces of g-C_3N_4, ZnO, GZ, GZA, g-C_3N_4_Carr, ZnO_Carr, GZ_Carr, and GZA_Carr accounts for their high efficiencies. Thus, the positively charged cationic dye MB can be adsorbed on the surface of the highly negatively charged nanomaterials via a strong electrostatic attraction. The electrostatic interaction enhanced the adsorptive property and, thus, the degradation efficiencies [82,83]. Due to the low bandgap energy of Ag_2O and its ability to absorb visible light, its incorporation influences the degradation [31,84] since Ag_2O acts as an efficient photosensitizer [30].

3.5.4. Degradation of methylene green

The efficiency of visible light MG degradation was confirmed in Fig. 7 (d). The g-C_3N_4, ZnO, GZ, GZA, Carr, g-C_3N_4_Carr, ZnO_Carr, GZ_Carr, GZA_Carr degraded 67.50 %, 55.33 %, 67.33 %, 91.49 %, 70.15 %, 68.11 %, 93.22 %, 98.93 % respectively, of MG dye. The adsorption of MG by g-C_3N_4 doesn't show a significant change in the amount of dye in the solution during the first 20 min. However, after 30 min, there is a noticeable drop in the solution's dye amount from 100 % to 80.33 %. This suggests that 19.67 % of the dye is adsorbed to g-C_3N_4, and as the visible light was irradicated, the photocatalytic process started, leading to the degradation of MG. The rapid drop in dye concentration indicates that the reaction rate increased. Over the next 30 min, there is a substantial reduction in the dye concentration, which drops from 80.33 % to 52.75 %. This indicates that the photocatalytic activity of g-C_3N_4 is effectively degrading the MG. After 60 min, the degradation rate seems to slow down during this period, as the dye concentration decreases gradually from 52.75 % to 45.07 %. The degradation rate continues to slow, with the dye concentration decreasing from 45.07 % to 33.50 % over the 120–210 min period. The data shows that the photocatalyst g-C_3N_4 effectively degrades methylene green over time. The initial delay in degradation might be due to the time required for the reaction to initiate. The rapid drop in dye concentration within the first 30 min indicates efficient adsorption activity. At the same time, the gradual decrease in the degradation rate suggests that factors like efficient photocatalytic activity, reaction kinetics, and catalyst activity play a role.

The nanocomposites with higher degradation efficiencies are GZA GZA_Carr, at 96.50 % and 96.76 %, respectively, with Ag_2O with a low degradation efficiency of 51.43 % at 210 min. On the other hand, g-C_3N_4_Carr, GA_Carr, and GZA_Carr showed improved degradation efficiency compared to their counterparts without carrageenan. The degradation rate is faster in the presence of GZA nanocomposites, which are more electronegative, hence having a high affinity towards the positively charged dye. In the MG, the ZnO had a lower degradation efficiency, but its efficiency was increased once combined with Ag_2O and g-C_3N_4. This illustrates the importance of combining nanocomposites to improve their performance by reducing their band gap and electronegativity.

Table 2
Comparison of GZA_Carr and GZA for the various degradation of organic pollutants.

Synthesis method	Material	Dye	Dosage of photocatalyst	Photocatalysis Efficiency (%)	Time (min)	Reference
Co-precipitation method	ZnO–SnO_2	Methylene blue, Rhodamine B, Trypan blue, Orange methylene and Yellow quinoline	200 mg in 60 mL solution in 18 mg/L dye	76.44, 72.69, 62.43, 77.00 and 92.46	60	[85]
Biosynthesis	ZnO	Congo red	8 mg in 1.5 mg/L dye	87	60	[63]
In-situ precipitation	HAp/g-C_3N_4	Methylene blue	50 mg	93.69	100	[41]
Hydrothermal	CeO_2/g-C_3N_4	2-Chlorophenol	50 mg in 30 mL of 20 mg/L dye solutions	84	100	[86]
Hydrothermal	g-C_3N_4/ZnO–Ag_2O	Methylene blue	50 mg in 100 mL of 30 mg/L dye solution	96.5	120	[2]
Hydrothermal	MoS_2–SnS_2@g–C_3N_4	Methylene blue	50 mg in 50 mL of 10 mg/L dye solution	86.60	90	[87]
Hydrothermal	g-C_3N_4/ ZnO–Ag_2O_Carr	Methylene blue, Congo red, methylene green, methyl violet	20 mg in 50 mL in 20 mg/L dye	95.81, 87.76, 96.50, 98.93	120	This work
Hydrothermal	g-C_3N_4/ZnO–Ag_2O	Methylene blue, Congo red, methylene green, methyl violet	20 mg in 50 mL in 20 mg/L dye	98.42, 83.49, 96.76, 91.48	120	This work

Table 3
Rate constants and coefficient of determination for photocatalytic degradation of Congo red, methylene violet, methylene blue and methylene green using the synthesized nanomaterials and nanocomposites.

Dyes	Congo Red				Methyl Violet				Methylene Blue				Methylene Green			
Nanomaterial	Pseudo 1st order		Pseudo 2nd order		Pseudo 1st order		Pseudo 2nd order		Pseudo 1st order		Pseudo 2nd order		Pseudo 1st order		Pseudo 2nd order	
	k	R^2	k	R^2	k	R^2	K	R^2	k	R^2	k	R^2		R^2	k	R^2
g-C_3N_4	0.0025	0.9956	0.3409	0.9823	0.0033	0.9770	0.2541	0.9932	0.0050	0.9762	0.2060	0.9942	0.0055	0.9633	0.1968	0.9694
ZnO	0.0022	0.9936	0.3658	0.9858	0.0038	0.9873	0.2445	0.9929	0.0051	0.9494	0.1850	0.9909	0.0042	0.9666	0.1286	0.9914
Ag_2O	0.00445	0.9929	0.2226	0.9848	0.0064	0.9642	0.1851	0.9969	0.0098	0.9539	0.1718	0.9910	0.0057	0.9636	0.1908	0.9976
GA	0.0016	0.9830	0.4622	0.9897	0.0029	0.9658	0.3096	0.9940	0.0067	0.9404	0.1831	0.9930	0.0033	0.9654	0.2975	0.9967
GZ	0.0046	0.9854	0.2533	0.9958	0.0038	0.9743	0.2468	0.9920	0.0187	0.9769	0.1273	0.9974	0.0046	0.9385	0.2156	0.9959
GZA	0.0092	0.9929	0.1573	0.9954	0.0116	0.9584	0.1518	0.9919	0.0190	0.9833	0.1328	0.993	0.0149	0.9479	0.1316	0.9946
g-C_3N_4_Carr	0.0056	0.9788	0.1904	0.9933	0.0042	0.9820	0.2412	0.9947	0.0167	0.9763	0.1328	0.9959	0.0085	0.9643	0.1599	0.9977
ZnO_Carr	0.0025	0.9965	0.3315	0.9954	0.0077	0.9647	0.1692	0.9839	0.0089	0.9799	0.1695	0.9982	0.0061	0.9565	0.1908	0.9917
Ag_2O_Carr	0.0055	0.9920	0.1920	0.9941	0.0106	0.9794	0.1474	0.9896	0.0185	0.9738	0.1247	0.9863	0.0129	0.9869	0.1408	0.9947
GA_Carr	0.0024	0.9783	0.3592	0.9940	0.0049	0.977	0.2335	0.9974	0.0102	0.9850	0.1429	0.9641	0.0056	0.9653	0.2064	0.9817
GZ_Carr	0.0031	0.9837	0.3183	0.9903	0.0058	0.954	0.1859	0.9899	0.0162	0.9690	0.1363	0.9902	0.0052	0.9877	0.2165	0.9971
GZA_Carr	0.0107	0.9885	0.1446	0.9982	0.0199	0.960	0.1291	0.9948	0.0151	0.9752	0.1298	0.9952	0.0175	0.9597	0.2490	0.9933

3.5.5. Comparative efficiency analysis of photocatalyst nanocomposites for organic pollutant degradation

In Table 2, a comparative analysis of the photocatalysis performance was presented for the prepared g-C_3N_4/ZnO/Ag_2O_Carrageenan photocatalyst with previously reported nanocomposites for the degradation of diverse dyes and organic pollutants. This comparison sheds light on the efficacy of this study's synthesized photocatalyst in achieving high degradation efficiencies with relatively lower quantities compared to existing alternatives. This presented that on the previously reported nanocomposites, a large amount of the photocatalysts was required to obtain a high degradation efficiency, whereas for GZA_Carr, 20 mg in 50 mL dye solution was sufficient for a ≥90 % dye degradation (see Table 3).

The synthesized photocatalyst, GZA_Carr, demonstrated notable superiority in terms of photocatalytic efficiency across a range of dyes compared to the other reported photocatalysts. The significant advantage lies in the reduced dosage required for effective dye degradation, highlighting the efficiency of our approach. Therefore, it can be inferred that the incorporation of Carr into the photocatalyst formulation enhanced adsorption capacity, thereby promoting increased contact between the pollutant and the nanomaterials, ultimately leading to enhanced degradation efficiency. The presented results underscore the novelty and efficacy of our synthesized photocatalyst, showcasing its potential for practical application in wastewater treatment and environmental remediation.

3.5.6. Kinetic studies

The photocatalysis kinetics of dyes were analyzed by pseudo-1st-order and pseudo-2nd-order kinetic models using equations (5) and (6) [43].

$$ln\frac{C_0}{C_t} = -kt \quad [7]$$

where C_0 represents the initial concentration, C_t is the concentration after a specific time, k represents the apparent rate constant of the photodegradation reaction, and t is time.

$$\frac{t}{qt} = \frac{1}{k_2 q_e^2} + \frac{1}{q_e} \quad [8]$$

Where q_e and q_t are the adsorption capacity at equilibrium and time t, respectively (mg/g), where k_2 is the rate constant of pseudo-2nd-

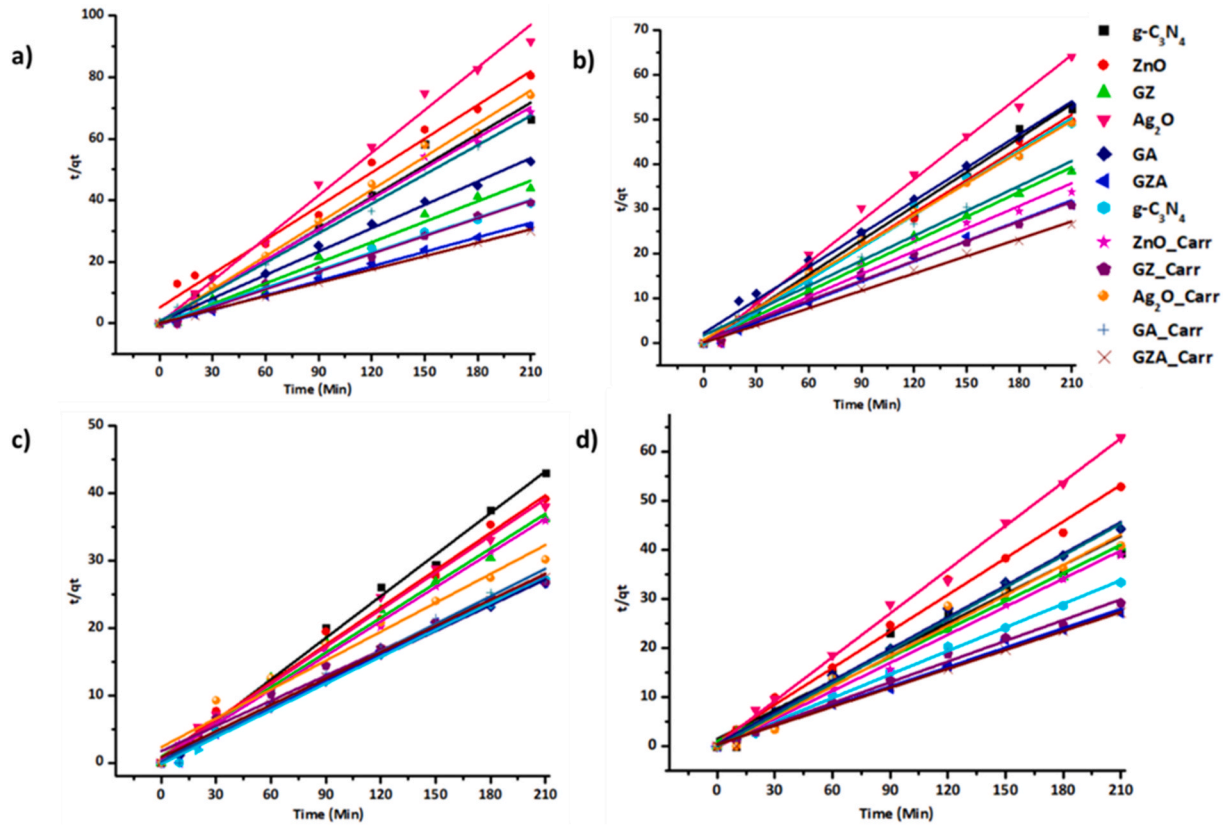

Fig. 9. Pseudo-2nd-order rate kinetics for photocatalytic degradation of a) Congo red, b) methylene violet, c) methylene blue, and d) methylene green using the synthesized nanomaterials and nanocomposites.

order.

Figs. 8 and 9 showed the linear relationships between $\ln(C_o/C_t)$ or t/qt and the irradiation time. Also, the rate constants and degradation efficiencies of CR, MV, MB and MG with different photocatalyst samples of nanocomposites are displayed in Table 2. The data indicates that the photocatalytic degradation of the dye is occurring over time, and the degradation rate is not the same on all the nanomaterials. For example, the pseudo-1st-order rate constant (k) values range from 0.00161 to 0.01069 on CR. Due to the higher pseudo-1st-order rate constant (k) (0.01069) of GZA_Carr, the degradation rate for CR was faster than that observed with the other photocatalysts, as depicted in Table 2. The GA had the lowest k constant, 0.00161. The Coefficient of Determination (R^2) values range from 0.97827 to 0.99649 for the pseudo-1st-order kinetics model of CR, which suggests that it fits the experimental data relatively well across all photocatalysts. Overall, the results show that these nanomaterials are effective photocatalysts for degrading all dyes under pseudo-1st-order kinetics and pseudo-2nd-order kinetics models. The differences in the rate constants could be attributed to the varying catalytic activities of the different nanomaterials [88,89]. From these rate constants in Tables 2 and it can be observed that MB has the highest pseudo-1st-order rate constant, and CR has the highest pseudo-2nd-order rate, indicating that it exhibits the fastest degradation when considering the influence of chemical interactions between dye molecules. The pseudo-2nd-order kinetics model implies that the interaction between multiple molecules of the dye influences the degradation of these dyes. In this model, the rate of degradation is proportional to the square of the concentration of the dye. Compared to the pseudo-1st-order model, the pseudo-2nd-order model often suggests a more significant role of chemical interactions, such as adsorption and chemical reactions, in the degradation process [88,89].

3.5.7. Recyclability

Since the GZA_Carr nanocomposites showed a higher degradation rate compared to the other nanocomposites, they were selected and used for recyclability. The reusability test results of GZA_Carr nanocomposites on methylene blue, Congo red, methylene green and methyl violet are demonstrated in Fig. 10b. It could be revealed that the as-obtained GZA_Carr nanocomposite had outstanding photo-degradation stability after five successive recycling across all dyes. For instance, on the first cycle, the degradation efficiency for MB, CR, MG, and MV were 95.81 % ± 1.19, 87.76 % ± 0.92, 96.50 % ± 1.17, and 98.93 % ± 1.17 respectively. After the 5 cycles, the GZA_Carr nanocomposites withstand the rewashing and reached 92.46 % ± 0.78, 85.15 % ± 1.14, 93.19 % ± 1.15, 95.62 % ± 0.99. Comparably, the degradation efficiency for MB, CR, MG, and MV for GZA on the 1st cycle were 98.42 % ± 1.16, 83.49 % ± 1.12, 96.76 % ± 0.75, 91.48 % ± 1.24. After 5 recycling the efficiencies were 95.14 % ± 0.76, 80.32 % ± 0.67, 94.65 % ± 0. 71, and 87.99 % ± 0.77. This showed that the GZA and GZA_Carr performed relatively well after 5 recycling, implying that they can be used for the removal of dyes multiple times.

The slight decline in photocatalytic performance may be attributed to the attachment of some dye molecules to the photocatalysts, hence reducing active sites [2,41,86,87]. However, still, these nanocomposites are economical since visible light was utilized which is affordable over UV sources thus the energy source can be used multiple times with less cost. Thus, it can be concluded that the nanocomposites can produce the same results through several cycles.

3.5.8. Mechanism of degradation of dyes

The proposed photocatalysis mechanism is illustrated in Fig. 11. The g-C_3N_4 acts as an electron pool, whereas ZnO and Ag_2O make the nanomaterial visible light suitable g-C_3N_4, ZnO and Ag_2O have band gaps of 2.7 eV, 3.3 eV and 1.3 eV respectively. However, once the nanocomposite of these nanomaterials is formed, the band gap is reduced as illustrated and discussed in section 3.3. This reduction in the band gap resulted in the reduction of the recombination rate [10,23,25].

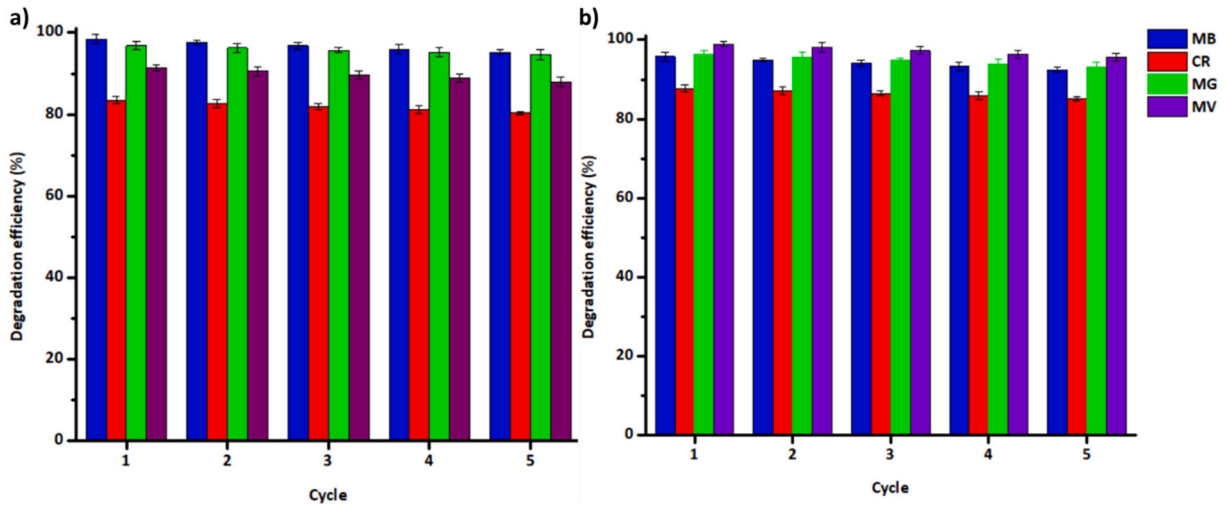

Fig. 10. Reusability test of a) g-C_3N_4/ZnO/Ag_2O and b) g-C_3N_4/ZnO/Ag_2O_Carr on methylene blue, Congo red, methylene green and methyl violet for five successive recycling runs.

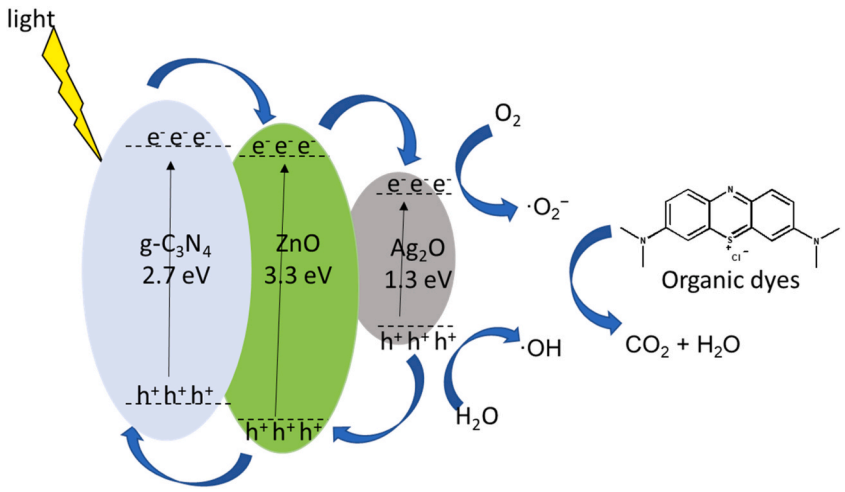

Fig. 11. Schematic representation of the photocatalytic mechanism of the g-C_3N_4/ZnO/Ag_2O (GZA) nanocomposite under visible light irradiation.

During photocatalysis, visible light was exposed to the nanomaterials. So, when the light hits the g-C_3N_4/ZnO/Ag_2O (GZA), reactive oxygen species are produced. These reactive oxygen species break down organic pollutants, producing O_2 and H_2O [25]. In short, photons excite electrons on the GZA, and the electrons are transferred to the conduction band of g-C_3N_4/ZnO/Ag_2O [25,90].

$$g - C_3N_4 \,/\, ZnO \,/\, Ag_2O \rightarrow g - C_3N_4 \,/\, ZnO \,/\, Ag_2O\,(h^+ + e^-) \tag{9}$$

Since the conduction band of g-C_3N_4 is more negative than ZnO and Ag_2O, the photogenerated electrons of g-C_3N_4 jump easily to the CB of ZnO and Ag_2O, as demonstrated in Fig. 11. The ZnO conduction band electrons can reduce oxygen (O_2) to obtain a highly active superoxide radical ion ($\bullet O_2^-$) [25].

$$ZnO\ and \,/\, Ag_2O(e^-) + dye + O_2 \rightarrow \bullet O_2^- \tag{10}$$

The $\bullet O_2^-$ then decomposes the organic dye into carbon dioxide and water. The hole (h+) in the g-C_3N_4 valence band oxidizes H_2O or –OH to obtain •OH, which further decomposes organic pollutants into carbon dioxide and water [25,90].

$$g - C_3N_4\,(h^+) + H_2O \,/\, OH^- \rightarrow \ \bullet\mathrm{OH} \tag{11}$$

$$\bullet O_2^- \ / \ \bullet\mathrm{OH} + \mathrm{dyes} \rightarrow \ CO_2 + H_2O \tag{12}$$

3.5.9. Future directions and potential in applications beyond dye degradation

Due to the success of the nanocomposites on the photocatalysis of dyes, it is projected that the nanocomposites can be used in the degradation of pharmaceuticals and other organic pollutants from water. Moreover, these nanocomposites were used in heavy metal adsorption because of their electronegativity; hence, they can withdraw positive pollutants onto their surface, and this will be reported in the future. In membrane technology, nanocomposites were incorporated into biopolymeric membranes to enhance the membranes' rejection capability and introduce photocatalytic properties.

4. Conclusion

This research has achieved significant success in the synthesis and characterization of innovative nanocomposite systems consisting of g-C_3N_4, ZnO, and Ag_2O nanomaterials embedded within a carrageenan matrix. Highly efficient photocatalytic nanocomposites of g-C_3N_4, ZnO, and Ag_2O were successfully synthesized through a combination of hydrothermal and chemical precipitation methods. The successful synthesis of the nanocomposites was confirmed by the characteristic peaks corresponding to Zn–O (590-404 cm^{-1}), Ag–O (2072 cm^{-1}), and triazine units (812 cm^{-1}) as observed from the FTIR spectra. Further validation through SEM-EDX and elemental mapping affirmed the presence of Zn, O, Ag, C, and N. The TEM imaging exhibited the nanosheet morphology for g-C_3N_4, nanorod structure for ZnO, and spherical form for the Ag_2O nanomaterials.

The incorporation of these nanocomposites into the carrageenan matrix resulted in unique sheet-like structures. Notably, the ZnO and Ag_2O nanomaterials consistently exhibited sizes within the range of 10–20 nm, demonstrating their effectiveness. The ability of these nanocomposites to harness visible light is evidenced by visible light emission in the 400–450 nm range upon excitation at 380 nm. Dye degradation under visible light, with remarkable efficiency levels ranging from 80 % to 98 %, was observed. For example, g-C_3N_4/ZnO/Ag_2O_Carr, which was a novel nanocomposite in this study, had a degradation efficiency of 95.81 %, 87.76 %, 96.50 %, 98.93 % on MB, CR, MG, and MV, respectively. These efficiencies were relatively higher than other composites for the same dye degradation. This was attributed to the synergistic interactions between the g-C_3N_4, ZnO, and Ag_2O after the irradiation with visible

light. These findings highlight the remarkable potential of these nanocomposites for a wide range of applications. Overall, this research represents a significant advancement in the field of environmentally friendly and stable nanocomposite materials, with promising prospects for addressing various challenges and opportunities in diverse fields.

Data availability

Data will be made available on request.

Funding

This work was supported by the University of Johannesburg's Centre for Nanomaterials Science Research.

CRediT authorship contribution statement

Feziwe B. Mamba: Writing – original draft, Validation, Project administration, Methodology, Investigation, Formal analysis, Data curation, Conceptualization. **Bhekani S. Mbuli:** Writing – review & editing, Visualization, Validation, Supervision, Software, Methodology, Investigation, Funding acquisition, Formal analysis, Data curation, Conceptualization. **James Ramontja:** Writing – review & editing, Visualization, Validation, Supervision, Software, Resources, Project administration, Investigation, Funding acquisition, Formal analysis, Data curation, Conceptualization.

Declaration of competing interest

The authors declare that they have no known competing financial interests or personal relationships that could have appeared to influence the work reported in this paper.

Acknowledgements

The University of Johannesburg's Centre for Nanomaterials Science Research provided funding, for which the authors are grateful of. The authors would like to extend their heartfelt gratitude to the DST/Mintek Nanotechnology Innovation Centre for providing the technical capacity required to carry out this research. Lastly, the authors are grateful to the University of Johannesburg, Faculty of Science, Department of Chemicals Sciences, for granting them a space to conduct the study.

References

[1] R. Al-Tohamy, S.S. Ali, F. Li, K.M. Okasha, Y.A.-G. Mahmoud, T. Elsamahy, H. Jiao, Y. Fu, J. Sun, A critical review on the treatment of dye-containing wastewater: ecotoxicological and health concerns of textile dyes and possible remediation approaches for environmental safety, Ecotoxicol. Environ. Saf. 231 (2022) 113160, https://doi.org/10.1016/j.ecoenv.2021.113160.

[2] S. Vignesh, P. Eniya, M. Srinivasan, J.K. Sundar, H. Li, S. Jayavel, M. Pandiaraman, M.A. Manthrammel, M. Shkir, B. Palanivel, Fabrication of Ag/Ag_2O incorporated graphitic carbon nitride based ZnO nanocomposite for enhanced Z-scheme photocatalytic performance of various organic pollutants and bacterial disinfection, J. Environ. Chem. Eng. 9 (5) (2021) 105996, https://doi.org/10.1016/j.jece.2021.105996.

[3] A. Azanaw, B. Birlie, B. Teshome, M. Jemberie, Textile effluent treatment methods and eco-friendly resolution of textile wastewater, Case Stud. Chem. Environ. Eng. 6 (2022) 100230, https://doi.org/10.1016/j.cscee.2022.100230.

[4] J. Sharma, S. Sharma, V. Soni, Classification and impact of synthetic textile dyes on Aquatic Flora: a review, Reg. Stud. Mar. Sci. 45 (2021) 101802, https://doi.org/10.1016/j.rsma.2021.101802.

[5] F. Parvin, S. Islam, S.I. Akm, Z. Urmy, S. Ahmed, A study on the solutions of environment pollution and worker's health problems caused by textile manufacturing operations, Biomed. J. Sci. Technol. Res. 28 (4) (2020) 21831–21844, https://doi.org/10.26717/BJSTR.2020.28.004692.

[6] M. Saeed, M. Muneer, N. Akram, Photocatalysis: an effective tool for photodegradation of dyes—a review, Environ. Sci. Pollut. Res. (2021) 1–19, https://doi.org/10.1007/s11356-021-16389-7.

[7] I. Zahoor, A. Mushtaq, Water pollution from agricultural activities: a critical global review, Int. J. Chem. Biochem. Sci 23 (2023) 164–176.

[8] D.R. Rout, H.M. Jena, O. Baigenzhenov, A. Hosseini-Bandegharaei, Graphene-based materials for effective adsorption of organic and inorganic pollutants: a critical and comprehensive review, Sci. Total Environ. 863 (2023) 160871, https://doi.org/10.1016/j.scitotenv.2022.160871.

[9] A. Kumar, A. Nighojkar, P. Varma, N.J. Prakash, B. Kandasubramanian, K. Zimmermann, F. Dixit, Algal mediated intervention for the retrieval of emerging pollutants from aqueous media, J. Hazard Mater. 455 (2023) 131568, https://doi.org/10.1016/j.jhazmat.2023.131568.

[10] S. Vignesh, P. Eniya, M. Srinivasan, J.K. Sundar, H. Li, S. Jayavel, M. Pandiaraman, M.A. Manthrammel, M. Shkir, B. Palanivel, Fabrication of Ag/Ag_2O incorporated graphitic carbon nitride based ZnO nanocomposite for enhanced Z-scheme photocatalytic performance of various organic pollutants and bacterial disinfection, J. Environ. Chem. Eng. 9 (5) (2021) 1–13, https://doi.org/10.1016/j.jece.2021.105996.

[11] J. Żur, A. Piński, A. Marchlewicz, K. Hupert-Kocurek, D. Wojcieszyńska, U. Guzik, Organic micropollutants paracetamol and ibuprofen—toxicity, biodegradation, and genetic background of their utilization by bacteria, Environ. Sci. Pollut. Control Ser. 25 (22) (2018) 21498–21524, https://doi.org/10.1007/s11356-018-2517-x.

[12] L. Xu, Z. Zhou, N.J. Graham, M. Liu, W. Yu, Enhancing ultrafiltration performance by gravity-driven up-flow slow biofilter pre-treatment to remove natural organic matters and biopolymer foulants, Water Res. 195 (2021) 1–12, https://doi.org/10.1016/j.watres.2021.117010.

[13] S. Ihaddaden, D. Aberkane, A. Boukerroui, D. Robert, Removal of methylene blue (basic dye) by coagulation-flocculation with biomaterials (bentonite and Opuntia ficus indica), J. Water Process Eng. 49 (2022) 102952, https://doi.org/10.1016/j.jwpe.2022.102952.

[14] L. Rahmawati, M.M. Azis, R. Rochmadi, In *Methylene blue removal from wastewater using sodium lignosulfonate and polyaluminium chloride: Optimization with RSM*, in: AIP Conference Proceedings, AIP Publishing LLC, 2021 020035, https://doi.org/10.1063/5.0052016.

[15] F. Mcyotto, Q. Wei, D.K. Macharia, M. Huang, C. Shen, C.W. Chow, Effect of dye structure on colour removal efficiency by coagulation, Chem. Eng. J. 405 (2021) 126674, https://doi.org/10.1016/j.cej.2020.126674.

[16] W. Ding, L. Zhao, H. Yan, X. Wang, X. Liu, X. Zhang, X. Huang, R. Hang, Y. Wang, X. Yao, Bovine serum albumin assisted synthesis of Ag/Ag_2O/ZnO photocatalyst with enhanced photocatalytic activity under visible light, Colloids Surf. A Physicochem. Eng. Asp. 568 (2019) 131–140, https://doi.org/10.1016/j.colsurfa.2019.02.015.

[17] H. Anwer, A. Mahmood, J. Lee, K.-H. Kim, J.-W. Park, A.C. Yip, Photocatalysts for degradation of dyes in industrial effluents: opportunities and challenges, Nano Res. 12 (5) (2019) 955–972, https://doi.org/10.1007/s12274-019-2287-0.

[18] F. Zhao, X. Li, M. Zuo, Y. Liang, P. Qin, H. Wang, Z. Wu, L. Luo, C. Liu, L. Leng, Preparation of photocatalysts decorated by carbon quantum dots (CQDs) and their applications: a review, J. Environ. Chem. Eng. (2023) 109487, https://doi.org/10.1016/j.jece.2023.109487.

[19] Y. Sun, D.W. O'Connell, Application of visible light active photocatalysis for water contaminants: a review, Water Environ. Res. 94 (10) (2022) e10781, https://doi.org/10.1002/wer.10781.

[20] P. Shanmugam, S.M. Smith, S. Boonyuen, A. Luengnaruemitchai, In-situ development of boron doped g-C3N4 supported SBA-15 nanocomposites for photocatalytic degradation of tetracycline, Environ. Res. 224 (2023) 115496, https://doi.org/10.1016/j.envres.2023.115496.

[21] N. Swarnkar, R.K. Yadav, S. Singh, R. Shahin, R.K. Shukla, S.K. Tripathi, D.K. Dwivedi, S. Nath, C. Singh, J.-O. Baeg, Highly selective in-situ prepared g-C3N4/PB composite photocatalyst for direct CH bond arylation and NADH regeneration cofactor under solar light, J. Chem. Sci. 135 (2) (2023) 29, https://doi.org/10.1007/s12039-023-02150-9.

[22] C. Yavuz, S.E. Ela, Fabrication of g-C_3N_4-reinforced CdS nanosphere-decorated TiO_2 nanotablet composite material for photocatalytic hydrogen production and dye-sensitized solar cell application, J. Alloys Compd. 936 (2023) 168209, https://doi.org/10.1016/j.jallcom.2022.168209.

[23] M. Joseph, N.K.M. Sadik, S.N. Remello, S. Haridas, S. De, Through space Sigma donation π acceptor assisted photocatalytic degradation of ciprofloxacin on TCPP supported g-C3N4, ChemistrySelect 8 (7) (2023) e202203348, https://doi.org/10.1002/slct.202203348.

[24] A. Alaghmandfard, K. Ghandi, A comprehensive review of graphitic carbon nitride (g-C_3N_4)–metal oxide-based nanocomposites: potential for photocatalysis and sensing, Nanomaterials 12 (2) (2022) 294, https://doi.org/10.3390/nano12020294.

[25] Q. Zhong, H. Lan, M. Zhang, H. Zhu, M. Bu, Preparation of heterostructure g-C_3N_4/ZnO nanorods for high photocatalytic activity on different pollutants (MB, RhB, Cr (VI) and eosin), Ceram. Int. 42 (2020) 12192–12199, https://doi.org/10.1016/j.ceramint.2020.01.265.

[26] V. Deepthi, B. Vidhya, T.A. Mathew, A. Sebastian, Investigation on ZnO nanorod array-based ZnO/SnSe and ZnO/CdSe thin film heterostructures for photocatalytic degradation of methylene blue, Mater. Lett. 331 (2023) 133370, https://doi.org/10.1016/j.matlet.2022.133370.

[27] S. Balu, S. Velmurugan, S. Palanisamy, S.-W. Chen, V. Velusamy, T.C. Yang, E.-S.I. El-Shafey, Synthesis of α-Fe_2O_3 decorated g-C_3N_4/ZnO ternary Z-scheme photocatalyst for degradation of tartrazine dye in aqueous media, J. Taiwan Inst. Chem. Eng. 99 (2019) 258–267, https://doi.org/10.1016/j.jtice.2019.03.011.

[28] H. Abdullah, D.-H. Kuo, Y.-R. Kuo, F.-A. Yu, K.-B. Cheng, Facile synthesis and recyclability of thin nylon film-supported n-type ZnO/p-type Ag_2O nanocomposite for visible light photocatalytic degradation of organic dye, J. Phys. Chem. C 120 (13) (2016) 7144–7154, https://doi.org/10.1021/acs.jpcc.5b12153.

[29] X. Chen, D.-H. Kuo, Y.-X. Hou, Enhancing the photodegradation of charged pollutants under visible light in Ag_2O/g-C_3N_4 catalyst by Coulombic interaction, J. Mater. Sci. 52 (9) (2017) 5147–5154, https://doi.org/10.1007/s10853-017-0751-0.

[30] D. Kulal, V.S. Kodialbail, Visible light mediated photocatalytic dye degradation using Ag_2O/AgO-TiO_2 nanocomposite synthesized by extracellular bacterial mediated synthesis-An eco-friendly approach for pollution abatement, J. Environ. Chem. Eng. 9 (4) (2021) 105389, https://doi.org/10.1016/j.jece.2021.105389.

[31] X. Rong, F. Qiu, Z. Jiang, J. Rong, J. Pan, T. Zhang, D. Yang, Preparation of ternary combined ZnO-Ag_2O/porous g-C_3N_4 composite photocatalyst and enhanced visible-light photocatalytic activity for degradation of ciprofloxacin, Chem. Eng. Res. Des. 111 (2016) 253–261, https://doi.org/10.1016/j.cherd.2016.05.010.

[32] H.A. Khalil, C.K. Saurabh, Y. Tye, T. Lai, A. Easa, E. Rosamah, M. Fazita, M. Syakir, A. Adnan, H. Fizree, Seaweed based sustainable films and composites for food and pharmaceutical applications: a review, R&SERev 77 (2017) 353–362, https://doi.org/10.1016/j.rser.2017.04.025.

[33] Y. Zheng, Y. Zhu, J. Dai, J. Lei, J. You, N. Chen, L. Wang, M. Luo, J. Wu, Atomically precise Au nanocluster-embedded carrageenan for single near-infrared light-triggered photothermal and photodynamic antibacterial therapy, Int. J. Biol. Macromol. 230 (2023) 123452, https://doi.org/10.1016/j.ijbiomac.2023.123452.

[34] P. Li, J.A. Terrett, J.R. Zbieg, Visible-light photocatalysis as an enabling technology for drug discovery: a paradigm shift for chemical reactivity, ACS Med. Chem. Lett. 11 (11) (2020) 2120–2130, https://doi.org/10.1021/acsmedchemlett.0c00436.

[35] Y. Yuan, L. Zhang, J. Xing, M.I.B. Utama, X. Lu, K. Du, Y. Li, X. Hu, S. Wang, A. Genç, High-yield synthesis and optical properties of g-C_3N_4, Nanoscale 7 (29) (2015) 12343–12350, https://doi.org/10.1039/c5nr02905h.

[36] X. Zhang, X. Xie, H. Wang, J. Zhang, B. Pan, Y. Xie, Enhanced photoresponsive ultrathin graphitic-phase C3N4 nanosheets for bioimaging, J. Am. Chem. Soc. 135 (1) (2013) 18–21, https://doi.org/10.1021/ja308249k.

[37] S. Yang, Y. Gong, J. Zhang, L. Zhan, L. Ma, Z. Fang, R. Vajtai, X. Wang, P.M. Ajayan, Exfoliated graphitic carbon nitride nanosheets as efficient catalysts for hydrogen evolution under visible light, Adv. Mater. 25 (17) (2013) 2452–2456, https://doi.org/10.1002/adma.201204453.

[38] S. Vijayanath, K. Janaki, Tailoring power conversion efficiency of dye-sensitized solar cell based on ZnO/g-C_3N_4 hybrid photoelectrodes via microwave irradiation route, Inorg. Chem. Commun. 120 (2020) 1–9, https://doi.org/10.1016/j.inoche.2020.108119.

[39] M.R. Nath, A.N. Ahmed, M.A. Gafur, M.Y. Miah, S. Bhattacharjee, ZnO nanoparticles preparation from spent zinc-carbon dry cell batteries: studies on structural, morphological and optical properties, J. Asian Ceram. Soc. 6 (3) (2018) 262–270, https://doi.org/10.1080/21870764.2018.1507610.

[40] A. Alshahrani, A. Alharbi, S. Alnasser, M. Almihdar, M. Alsuhybani, B. AlOtaibi, Enhanced heavy metals removal by a novel carbon nanotubes buckypaper membrane containing a mixture of two biopolymers: chitosan and i-carrageenan, Sep. Purif. Technol. 276 (2021) 1–9, https://doi.org/10.1016/j.seppur.2021.119300.

[41] P. Govindasamy, B. Kandasamy, P. Thangavelu, S. Barathi, M. Thandavarayan, M. Shkir, J. Lee, Biowaste derived hydroxyapatite embedded on two-dimensional g-C_3N_4 nanosheets for degradation of hazardous dye and pharmacological drug via Z-scheme charge transfer, Sci. Rep. 12 (1) (2022) 11572, https://doi.org/10.1038/s41598-022-15799-y.

[42] M. Oprea, S.I. Voicu, Cellulose acetate-based membranes for the removal of heavy metals from water in the context of circular economy, Industrial Crops Products 206 (2023) 117716, https://doi.org/10.1016/j.indcrop.2023.117716.

[43] T.H. Do, V.T. Nguyen, Q.D. Nguyen, M.N. Chu, T.C.Q. Ngo, L.V. Tan, Equilibrium, kinetic and thermodynamic studies for sorption of phosphate from aqueous solutions using ZnO nanoparticles, Processes 8 (11) (2020) 1397, https://doi.org/10.3390/pr8111397.

[44] I. Benisti, F. Shaik, Z. Xing, A. Ben-Rafael, L. Amirav, Y. Paz, The effect of Pt cocatalyst on the performance and transient IR spectrum of photocatalytic g-C_3N_4 nanospheres, Appl. Surf. Sci. 542 (2021) 148432, https://doi.org/10.1016/j.apsusc.2020.148432.

[45] A. Sett, D. Das, D. Banerjee, U. Ghorai, N. Das, B. Das, K. Chattopadhyay, 1D–2D hybrids as efficient optoelectronic materials: a study on graphitic carbon nitride nanosheets wrapped with zinc oxide rods, Dalton Trans. 47 (13) (2018) 4501–4507, https://doi.org/10.1039/c8dt00016f.

[46] A. Mohammadi, A. Aliakbarzadeh Karimi, Methylene blue removal using surface-modified TiO_2 nanoparticles: a comparative study on adsorption and photocatalytic degradation, J. Water Environ. Nanotechnol 2 (2) (2017) 118–128, https://doi.org/10.22090/jwent.2017.02.007.

[47] F.H.H. Abdellatif, M.M. Abdellatif, Bio-based i-carrageenan aerogels as efficient adsorbents for heavy metal ions and acid dye from aqueous solution, Cellulose 27 (1) (2020) 441–453, https://doi.org/10.1007/s10570-019-02818-x.

[48] D.A. Agostinho, A.I. Paninho, T. Cordeiro, A.V. Nunes, I.M. Fonseca, C. Pereira, A. Matias, M.G. Ventura, Properties of κ-carrageenan aerogels prepared by using different dissolution media and its application as drug delivery systems, Mater. Chem. Phys. 253 (2020) 1–11, https://doi.org/10.1016/j.matchemphys.2020.123290.

[49] G.S. Paul Dr, P. Panchal, S.P. Nehra, P. Choudhary, A. Sharma, ZnO-Modified gC_3N_4: a Potential photocatalyst for environmental application, ACS Omega 5 (8) (2020) 3828–3838, https://doi.org/10.1021/acsomega.9b02688.

[50] A. Taufik, S. Prakoso, R. Saleh, In microwave-assisted synthesis Ag_2O/TiO2/CeO2 for highly efficient photocatalyst, in: IOP Conf. Ser.: Mater. Sci. Eng., IOP Publishing, 2019 012008, https://doi.org/10.1088/1757-899X/496/1/012008.

[51] V. Manikandan, P. Velmurugan, J.-H. Park, W.-S. Chang, Y.-J. Park, P. Jayanthi, M. Cho, B.-T. Oh, Green synthesis of silver oxide nanoparticles and its antibacterial activity against dental pathogens, 3 Biotech 7 (1) (2017) 72, https://doi.org/10.1007/s13205-017-0670-4.

[52] A.A. Abd El Khalk, M.A. Betiha, A.S. Mansour, M.G. Abd El Wahed, A.M. Al-Sabagh, High degradation of methylene blue using A new nanocomposite based on zeolitic imidazolate framework-8, ACS Omega 6 (40) (2021) 26210–26220, https://doi.org/10.1021/acsomega.1c03195.

[53] A.Y. Zerga, M. Tahir, H. Alias, N. Kumar, Fuels, Titanium carbide MXenes cocatalyst with graphitic carbon nitride for photocatalytic H_2 production, CO_2 reduction, and reforming applications: a review on fundamentals and recent advances, Energy 37 (17) (2023) 12623–12664, https://doi.org/10.1021/acs.energyfuels.3c01887.

[54] F. Wei, H. Xing, Z. Xiu, J. Li, D. Xing, X. Han, Z-scheme TiO_2-Au@CN heterojunction for simultaneous water purification of disinfection and organic pollutant removal by simulated solar light, Mater. Res. Bull. 168 (2023) 112450, https://doi.org/10.1016/j.materresbull.2023.112450.

[55] H.K. Verma, D. Rehani, S.N. Sharma, K. Maurya, Synthesized zinc oxide nanorods and flowers studies for optical, di-electrical and photocatalytic applications, Optik 204 (2020) 164154, https://doi.org/10.1016/j.ijleo.2019.164154.

[56] A. Adewuyi, W.J. Lau, Nanomaterial development and its applications for emerging pollutant removal in water, in: W.J. Lau, K. Faungnawakij, K. Piyachomkwan, U.R. Ruktanonchai (Eds.), Handbook of Nanotechnology Applications, Elsevier, Amsterdam, Netherlands, 2021, pp. 67–97, https://doi.org/10.1016/B978-0-12-821506-7.00003-X.

[57] M.I. Said, A. Othman, Structural, optical and photocatalytic properties of mesoporous CuO nanoparticles with tunable size and different morphologies, RSC Adv. 11 (60) (2021) 37801–37813, https://doi.org/10.1039/d1ra04780a.

[58] P. Pascariu, C. Gherasim, A. Airinei, Metal oxide nanostructures (MONs) as photocatalysts for ciprofloxacin degradation, Int. J. Mol. Sci. 24 (11) (2023) 9564, https://doi.org/10.3390/ijms24119564.

[59] S. Yu, H. Pang, S. Huang, H. Tang, S. Wang, M. Qiu, Z. Chen, H. Yang, G. Song, D. Fu, Recent advances in metal-organic framework membranes for water treatment: a review, Sci. Total Environ. 800 (2021) 149662, https://doi.org/10.1016/j.scitotenv.2021.149662.

[60] P. Feng, Y. Kong, M. Liu, S. Peng, C. Shuai, Dispersion strategies for low-dimensional nanomaterials and their application in biopolymer implants, Materials Today Nano 15 (2021) 100127, https://doi.org/10.1016/j.mtnano.2021.100127.

[61] J.-H. Zhao, C.-J. Liu, Z.-H. Lv, Photoluminescence of ZnO nanoparticles and nanorods, Optik 127 (3) (2016) 1421–1423, https://doi.org/10.1016/j.ijleo.2015.11.018.

[62] N. Alhokbany, T. Ahamad, S.M. Alshehri, Fabrication of highly porous ZnO/Ag_2O nanoparticles embedded in N-doped graphitic carbon for photocatalytic degradation of tetracycline, J. Environ. Chem. Eng. 10 (3) (2022) 107681, https://doi.org/10.1016/j.jece.2022.107681.

[63] A. Ekennia, D. Uduagwu, O. Olowu, O. Nwanji, O. Oje, B. Daniel, S. Mgbii, C. Emma-Uba, Biosynthesis of zinc oxide nanoparticles using leaf extracts of Alchornea laxiflora and its tyrosinase inhibition and catalytic studies, Micron 141 (2021) 102964, https://doi.org/10.1016/j.micron.2020.102964.

[64] A.C. Ekennia, D.N. Uduagwu, N.N. Nwaji, O.O. Oje, C.O. Emma-Uba, S.I. Mgbii, O.J. Olowo, O.L. Nwanji, Green synthesis of biogenic zinc oxide nanoflower as a dual agent for photodegradation of an organic dye and tyrosinase inhibitor, J. Inorg. Organomet. Polym. Mater. 31 (2) (2021) 886–897, https://doi.org/10.1007/s10904-020-01729-w.

[65] J. Yerima, A. Babangida, S. Ezike, W. Dunama, A. Ahmed, Matrix method of determining optical energy bandgap of natural dye extracts, J. Appl. Sci. Environ. Manag. 26 (5) (2022) 943–948, https://doi.org/10.4314/jasem.v26i5.22.

[66] M.J. Hakimi-Tehrani, S. Hassanzadeh-Tabrizi, N. Koupaei, A. Saffar-Teluri, M. Rafiei, Facile thermal synthesis of g–C3N4/ZnO nanocomposite with antibacterial properties for photodegradation of Methylene blue, Mater. Res. Express 8 (12) (2021) 125002, https://doi.org/10.1088/2053-1591/ac3c71.

[67] D.R. Paul, S. Gautam, P. Panchal, S.P. Nehra, P. Choudhary, A. Sharma, ZnO-modified g-C3N4: a potential photocatalyst for environmental application, ACS Omega 5 (8) (2020) 3828–3838, https://doi.org/10.1021/acsomega.9b02688.

[68] N. Chidhambaram, K. Ravichandran, Fabrication of ZnO/g-C_3N_4 nanocomposites for enhanced visible light driven photocatalytic activity, Mater. Res. Express 4 (7) (2017) 075037, https://doi.org/10.1088/2053-1591/aa7abd.

[69] L. Wang, B. Cheng, L. Zhang, J. Yu, In situ irradiated XPS investigation on S-scheme TiO2@ ZnIn2S4 photocatalyst for efficient photocatalytic CO2 reduction, Small 17 (41) (2021) 2103447, https://doi.org/10.1002/smll.202103447.

[70] E. Sindhuja, K. Ravichandran, Cost-effective fabrication of (g-C_3N_4 + Mo) added photostable ZnO thin films for enhanced visible light responsive photocatalytic dye degradation, Mater. Res. Bull. 103 (2018) 299–308, https://doi.org/10.1016/j.materresbull.2018.03.007.

[71] Q. Li, M. Anpo, X. Wang, Application of photoluminescence spectroscopy to elucidate photocatalytic reactions at the molecular level, Res. Chem. Intermed. 46 (10) (2020) 4325–4344, https://doi.org/10.1007/s11164-020-04209-5.

[72] W.A. Nimpoeno, H.O. Lintang, L. Yuliati, In *Zinc oxide with visible light photocatalytic activity originated from oxygen vacancy defects*, in: IOP Conf. Ser.: Mater. Sci. Eng., IOP Publishing, 2020 012080, https://doi.org/10.1088/1757-899X/833/1/012080.

[73] V. Etacheri, C. Di Valentin, J. Schneider, D. Bahnemann, S.C. Pillai, Visible-light activation of TiO_2 photocatalysts: advances in theory and experiments, J. Photochem. Photobiol. C Photochem. Rev. 25 (2015) 1–29.

[74] S. Abdolhosseinzadeh, H. Asgharzadeh, S. Sadighikia, A. Khataee, UV-assisted synthesis of reduced graphene oxide–ZnO nanorod composites immobilized on Zn foil with enhanced photocatalytic performance, Res. Chem. Intermed. 42 (2016) 4479–4496, https://doi.org/10.1007/s11164-015-2291-z.

[75] L. Saikia, D. Bhuyan, M. Saikia, B. Malakar, D.K. Dutta, P. Sengupta, Photocatalytic performance of ZnO nanomaterials for self sensitized degradation of malachite green dye under solar light, Appl. Catal. A: Gen. 490 (2015) 42–49, https://doi.org/10.1016/j.apcata.2014.10.053.

[76] W. Li, G. Wang, C. Chen, J. Liao, Z. Li, Enhanced visible light photocatalytic activity of ZnO nanowires doped with Mn^{2+} and Co^{2+} Ions, Nanomaterials 7 (20) (2017), https://doi.org/10.3390/nano7010020.

[77] F. Azeez, E. Al-Hetlani, M. Arafa, Y. Abdelmonem, A.A. Nazeer, M.O. Amin, M. Madkour, The effect of surface charge on photocatalytic degradation of methylene blue dye using chargeable titania nanoparticles, Sci. Rep. 8 (1) (2018) 1–9, https://doi.org/10.1038/s41598-018-25673-5.

[78] R. Abazari, A.R. Mahjoub, S. Sanati, Z. Rezvani, Z. Hou, H. Dai, Ni-Ti layered double hydroxide@ graphitic carbon nitride nanosheet: a novel nanocomposite with high and ultrafast sonophotocatalytic performance for the degradation of antibiotics, Inorg. Chem. Commun. 58 (3) (2019) 1834–1849, https://doi.org/10.1021/acs.inorgchem.8b02575.

[79] A.U. Islam, M.M. Iqbal, M. Imran, M.A. Tariq, M. Nadeem, M.Q. Kakar, M. Nawaz, M. Amjad, S.A. Qaisrani, M. Rizwan, Potential of fish scale biochar nanocomposite with ZnO for effective sequestration of Cr (VI) from water: modeling and kinetics, Int. J. Environ. Res. 16 (4) (2022) 1–13, https://doi.org/10.1007/s41742-022-00432-7.

[80] X. Wei, H. Liu, T. Li, Z. Jiang, W. Hu, Q. Niu, J. Chen, Three-dimensional flower heterojunction g-C3N4/Ag/ZnO composed of ultrathin nanosheets with enhanced photocatalytic performance, J. Photochem. Photobiol., A: Chem 390 (2020) 112342, https://doi.org/10.1016/j.jphotochem.2019.112342.

[81] D. Kaur, V. Bagga, N. Behera, B. Thakral, A. Asija, J. Kaur, S. Kaur, SnSe/SnO 2 nanocomposites: a novel material for photocatalytic degradation of industrial waste dyes, Adv. Compos. Hybrid Mater. 2 (2019) 763–776, https://doi.org/10.1007/s42114-019-00130-7.

[82] Y. Guo, S. Huang, Y. Guo, Z. Ye, J. Nan, Q. Zhou, Y. Zhu, Efficient degradation of organic pollutants by enhanced interfacial internal electric field induced via various crystallinity carbon nitride homojunction, Appl. Catal. B Environ. 312 (2022) 121388, https://doi.org/10.1016/j.apcatb.2022.121388.

[83] H. Lei, X. Cui, X. Jia, J. Qi, Z. Wang, W. Chen, Enhanced tribocatalytic degradation of organic pollutants by ZnO nanoparticles of high crystallinity, Nanomaterials 13 (1) (2022) 46, https://doi.org/10.3390/nano13010046.

[84] V. Shetty, Solar light active biogenic titanium dioxide embedded silver oxide (AgO/Ag2O@ TiO2) nanocomposite structures for dye degradation by photocatalysis, Mater. Sci. Semicond. Process. 132 (2021) 105923, https://doi.org/10.1016/j.mssp.2021.105923.

[85] O. Długosz, A. Staroń, P. Brzoza, M. Banach, Synergistic effect of sorption and photocatalysis on the degree of dye removal in single and multicomponent systems on ZnO-SnO_2, Environ. Sci. Pollut. Res. 29 (18) (2022) 27042–27050, https://doi.org/10.1007/s11356-021-18044-7.

[86] D. Barathi, N. Rajalakshmi, R. Ranjith, R. Sangeetha, S. Meyvel, Controllable synthesis of CeO_2/g-C_3N_4 hybrid catalysts and its structural, optical and visible light photocatalytic activity, Diam. Relat. Mater. 111 (2021) 108161, https://doi.org/10.1016/j.diamond.2020.108161.

[87] K. Tamilarasu, R. Ranjith, A. Priyadharsan, T. Rojviroon, P. Maadeswaran, S. Suganya, C. Umarani, Hierarchical MOS_2–SNS_2@ g–C_3N_4 nanocomposite as an efficient and sustainable material for environmental remediation, J. Cluster Sci. 35 (2023) 561–573, https://doi.org/10.1007/s10876-023-02498-5.

[88] H.N. Bhatti, Y. Safa, S.M. Yakout, O.H. Shair, M. Iqbal, A. Nazir, Efficient removal of dyes using carboxymethyl cellulose/alginate/polyvinyl alcohol/rice husk composite: adsorption/desorption, kinetics and recycling studies, Int. J. Biol. Macromol. 150 (2020) 861–870, https://doi.org/10.1016/j.ijbiomac.2020.02.093.
[89] A. Akhmetzhan, N. Abeu, S.N. Longinos, A. Tashenov, N. Myrzakhmetova, N. Amangeldi, Z. Kuanyshova, Z. Ospanova, Z. Toktarbay, Synthesis and heavy-metal sorption studies of N, N-dimethylacrylamide-based hydrogels, Polymers 13 (18) (2021) 3084, https://doi.org/10.3390/polym13183084.
[90] M.I. Litter, Mechanisms of removal of heavy metals and arsenic from water by TiO_2-heterogeneous photocatalysis, in: Pure and Applied Chemistry, vol. 87, 2015, pp. 557–567, https://doi.org/10.1515/pac-2014-0710.